


**RESEARCH ARTICLE**

# Conductive and injectable hyaluronic acid/gelatin/gold nanorod hydrogels for enhanced surgical translation and bioprinting

Emi A. Kiyotake<sup>1</sup>  | Emily E. Thomas<sup>2</sup>  | Hannah B. Homburg<sup>3</sup> |  
Camille K. Milton<sup>3</sup> | Adam D. Smitherman<sup>4</sup> | Nathan D. Donahue<sup>1</sup> |  
Kar-Ming Fung<sup>5</sup> | Stefan Wilhelm<sup>1</sup> | Michael D. Martin<sup>3</sup> | Michael S. Detamore<sup>1</sup>

<sup>1</sup>Stephenson School of Biomedical Engineering, University of Oklahoma, Norman, Oklahoma, USA

<sup>2</sup>Department of Biomedical Engineering, University of Michigan, Ann Arbor, Michigan, USA

<sup>3</sup>Department of Neurosurgery, University of Oklahoma Health Sciences Center, Oklahoma City, Oklahoma, USA

<sup>4</sup>Department of Neurosurgery, Rush University Medical Center, Chicago, Illinois, USA

<sup>5</sup>Department of Pathology, University of Oklahoma Health Sciences Center, Oklahoma City, Oklahoma, USA

**Correspondence**

Michael S. Detamore, Stephenson School of Biomedical Engineering, University of Oklahoma, 173 Felgar St., Gallogly Hall Room 105, Norman, OK 73019, USA.  
Email: detamore@ou.edu

**Funding information**

National Institute of General Medical Sciences, Grant/Award Number: Institutional Development Award / #P20 GM103639; Office of Integrative Activities, Grant/Award Number: Major Research Instrumentation Program / #1828234; University of Oklahoma, Grant/Award Number: Stephenson Graduate Fellowship; National Institute of General Medical Sciences of the National Institutes of Health, Grant/Award Number: P20 GM103639; National Science Foundation (NSF) Major Research Instrumentation (MRI) Program, Grant/Award Number: #1828234

**Abstract**

There is growing evidence indicating the need to combine the rehabilitation and regenerative medicine fields to maximize functional recovery after spinal cord injury (SCI), but there are limited methods to synergistically combine the fields. Conductive biomaterials may enable synergistic combination of biomaterials with electric stimulation (ES), which may enable direct ES of neurons to enhance axon regeneration and reorganization for better functional recovery; however, there are three major challenges in developing conductive biomaterials: (1) low conductivity of conductive composites, (2) many conductive components are cytotoxic, and (3) many conductive biomaterials are pre-formed scaffolds and are not injectable. Pre-formed, non-injectable scaffolds may hinder clinical translation in a surgical context for the most common contusion-type of SCI. Alternatively, an injectable biomaterial, inspired by lessons from bioinks in the bioprinting field, may be more translational for contusion SCIs. Therefore, in the current study, a conductive hydrogel was developed by incorporating high aspect ratio citrate-gold nanorods (GNRs) into a hyaluronic acid and gelatin hydrogel. To fabricate nontoxic citrate-GNRs, a robust synthesis for high aspect ratio GNRs was combined with an indirect ligand exchange to exchange a cytotoxic surfactant for nontoxic citrate. For enhanced surgical placement, the hydrogel precursor solution (i.e., before crosslinking) was paste-like, injectable/bioprintable, and fast-crosslinking (i.e., 4 min). Finally, the crosslinked hydrogel supported the adhesion/viability of seeded rat neural stem cells in vitro. The current study developed and characterized a GNR conductive hydrogel/bioink that provided a refinable and translational platform for future synergistic combination with ES to improve functional recovery after SCI.

**KEYWORDS**

bioprinting, conductive biomaterial, gold nanorods, injectable spinal cord injury

## 1 | INTRODUCTION

Spinal cord injury (SCI) affects 294,000 people in the United States currently, with 17,800 new patients every year.<sup>1</sup> Functional recovery is uncommon after SCI with current clinical treatments. There are two main approaches to promote functional recovery after SCI: (1) rehabilitation approaches (e.g., motor training, electrical stimulation [ES]) and (2) regenerative medicine approaches (e.g., cells, drugs, biologics, scaffolds). For SCI, rehabilitative and regenerative medicine approaches *individually* have not yet resulted in full functional recovery in humans, and each has limitations.<sup>2</sup> The combination of regenerative medicine and rehabilitation, known as *regenerative rehabilitation*,<sup>3</sup> may be needed for full functional recovery. First, regenerative medicine may be needed to regenerate the axonal pathways, and second, rehabilitation approaches may be needed to promote functionality of the axons. Several *in vivo* studies<sup>4,5</sup> using regenerative rehabilitation have already produced better outcomes for nerve regeneration after SCI; however, there are few clinical trials for SCI using regenerative rehabilitation (e.g., cells + motor training [clinicaltrials.gov: NCT03979742, NCT03225625], scaffold + EES [NCT03966794]). Ultimately, there is a need for regenerative medicine approaches to be translated for use in the clinic and to be developed to complement and enhance rehabilitation approaches.

Therefore, the focus of the studies here was to develop a conductive biomaterial that, in the future, would be able to synergize and enhance rehabilitation approaches, and specifically the use of ES.<sup>2</sup> Conductive biomaterials (and biomaterials in general) have the potential to replace/reduce the inhibitory environment that prevents axon regeneration, which rehabilitative approaches typically cannot accomplish. However, conductive biomaterials (a regenerative approach) *combined* with ES and motor training (rehabilitative approaches) have the potential to better deliver ES directly to neurons (as compared to traditional nonconductive biomaterials), which may simultaneously promote axon regeneration and neural plasticity for enhanced functional recovery.<sup>6,7</sup> Conductive materials and ES combined have improved *in vitro* differentiation and neurite growth,<sup>8</sup> and may be able to regenerate damaged axons *in vivo*. Furthermore, ES after tissue regeneration may facilitate reorganization of intact spinal networks with the regenerated axons and promote better functional recovery.

There are three major challenges in developing conductive biomaterials: (1) low conductivity of conductive composites, (2) most conductive components are cytotoxic, and (3) most conductive biomaterials are pre-formed scaffolds, which may have limited surgical translation. First, given that most biomaterials are insulators, conductive composites (in the semi-conductor range) have typically been created by combining biomaterials with added conductive components (e.g., carbon-based structures, conductive polymers, metallic-based particles<sup>2</sup>). Gold nanoparticle-based composites have been widely investigated for tissue engineering purposes, particularly in cardiac, muscle, and peripheral nerve applications. Specifically, gold nanorod (GNR) biomaterials are promising conductive biomaterials that have

been developed and used for cardiac tissue engineering,<sup>9-12</sup> but have not yet been applied to SCI.

The second major challenge is eliminating the cytotoxicity of the CTAB surfactant required for shape control and rod formation during the synthesis of GNRs.<sup>13</sup> Given that GNR containing biomaterials will eventually release the GNRs after *in vivo* degradation, any remaining CTAB may potentially cause toxic *in vivo* side effects. Direct ligand exchange is commonly used to replace nanoparticle stabilizers or coatings; however, direct ligand exchange has low efficacy because CTAB binds more strongly to gold than common nontoxic ligands (e.g., citrate, polyethylene glycol [PEG]). Indirect ligand exchanges have been successful in replacing the cytotoxic CTAB with citrate,<sup>14</sup> but have not yet been applied *in vitro* or *in vivo*.

The third major challenge is the surgical placement of the biomaterial. GNR biomaterials (and biomaterials in general) are typically pre-formed solid scaffolds, which generally may not be relevant to a human contusion SCI with ill-defined borders. Injectable hydrogel precursors (i.e., before crosslinking) that can form a hydrogel under biological conditions within the injury (i.e., crosslinked *in situ*) are well-suited for surgical placement in a translational context for SCI. Unfortunately, hydrogel precursors are traditionally less viscous and leak out of the injury before crosslinking. To aid in placement and retention of hydrogel precursors within an injury, a more viscous or paste-like rheology of the precursor is needed, and we therefore draw inspiration from bioinks from the extrusion bioprinting field.<sup>15,16</sup>

The purpose of the current study was to fabricate a translational biomaterial platform for SCI by developing a hydrogel that was (1) conductive once crosslinked, (2) not cytotoxic, and (3) possessed an injectable and paste-like precursor. In the current study, we synthesized high aspect ratio, citrate capped-GNRs (citrate-GNRs) and incorporated them into a bioprintable hydrogel formulation comprised of pentenoate-functionalized hyaluronic acid (PHA) and pentenoate-functionalized gelatin (PGel). We evaluated the conductivity and ability of the GNR hydrogels to support the adhesion and viability of rat neural stem cells (rNSCs). We characterized the rheology of the GNR hydrogel precursor for evaluating the injectability and paste-like consistency for both, translatability and printability.

## 2 | MATERIALS AND METHODS

### 2.1 | Materials

Gold(III) chloride trihydrate ( $\text{HAuCl}_4$ ,  $\geq 99.9\%$ ), hexadecyltrimethylammonium bromide (CTAB) ( $\geq 99\%$ ), hydrochloric acid (HCl, 37%), hydroquinone ( $\geq 99.0\%$ ), nitric acid ( $\text{HNO}_3$ , 70%), polyvinylpyrrolidone (PVP,  $M_w$ : 55,000), silver nitrate ( $\text{AgNO}_3$ ,  $\geq 99\%$ ), sodium borohydride ( $\text{NaBH}_4$ , 99%), sodium hydroxide ( $\text{NaOH}$ ,  $\geq 98\%$ ), hydrogen peroxide ( $\text{H}_2\text{O}_2$ , 30%), L-ascorbic acid (AA,  $\geq 98\%$ ), sodium citrate tribasic dihydrate ( $\geq 99\%$ ) and all other chemicals were purchased from Sigma-Aldrich (St. Louis, Missouri) unless otherwise noted. Acetone ( $\geq 99.5\%$ ) was purchased from VWR (Radnor,

Pennsylvania). All reagents for gold nanorod synthesis were prepared with nanopure water from a Purist Pro UV Ultrapure Water System (RephiLe Bioscience, Ltd., Boston, Massachusetts) and prepared fresh daily except for  $\text{HAuCl}_4$  and  $\text{NaOH}$ . All glassware and Teflon-coated stir bars were cleaned with aqua regia (3:1 v/v  $\text{HCl}:\text{HNO}_3$ ) and rinsed 15 times with nanopure water before each synthesis.

## 2.2 | GNR synthesis

High aspect ratio CTAB-capped GNRs (CTAB-GNRs) were synthesized using a seed mediated growth method<sup>17</sup> (see illustration in Figure 1A). The seed solution consisted of CTAB (5 ml, 0.1 M),  $\text{HAuCl}_4$  (50  $\mu\text{l}$ , 50 mM), and ice-cold (liquid, not solid)  $\text{NaBH}_4$  (230  $\mu\text{l}$ , 0.01 M) added quickly and under vigorous stirring for 15–20 min. The growth solution consisted of CTAB (100 ml, 0.1 M),  $\text{HAuCl}_4$  (1 ml, 50 mM),  $\text{AgNO}_3$  (700  $\mu\text{l}$ , 0.1 M), hydroquinone (5 ml, 0.1 M), and seed solution (160  $\mu\text{l}$ ), and was left for 12 h in a 30°C water bath. GNRs were centrifuged (13,500 $\times$ g, 20 min) and washed with PVP (112 mM) to prevent aggregation. For additional details, see the Data S1. GNR formation was confirmed via UV-Vis-NIR and transmission electron microscopy (TEM), as described below.

## 2.3 | Citrate-GNRs via indirect ligand exchange

The CTAB on CTAB-GNRs was replaced with trisodium citrate through an indirect ligand exchange protocol<sup>14</sup> (see illustration in Figure 1B), with minor modifications: initial GNR concentration (0.38 mg/ml), Ag:Au ratio (0.158:1). To coat CTAB-GNRs with silver, a solution of PVP (144 ml, 47 mM), CTAB-GNRs (30 ml, 0.38 mg/ml), AA (3 ml, 40 mM), and  $\text{AgNO}_3$  (30 ml, 0.3 mM) was stirred (10 min, room temperature). Acetone (414 ml) was added, followed by centrifugation (13,500 $\times$ g, 10 min). Acetone was decanted, and the loose GNR pellets were sonicated (1 min) using a Branson 3800 Ultrasonic Cleaner (Cleanasonic, Richmond, Virginia) and re-dispersed in sodium citrate (6 ml, 10 mM). To etch away the silver and CTAB, 3%  $\text{H}_2\text{O}_2$  (27 ml) was added to the sodium citrate solution (3 h, room temperature). The solution was centrifuged (13,500 $\times$ g, 15 min) and re-dispersed in sodium citrate (3 ml, 10 mM) (12 h, room temperature). For additional details, see the Data S1. Citrate-capping of GNRs (citrate-GNRs) was confirmed with zeta potential measurements and gel electrophoresis, as described in the GNR Characterization section. For in vitro and in vivo studies, citrate-GNRs were diluted to 100 ml before being sterile-filtered using a Steriflip PLUS membrane (MilliporeSigma,

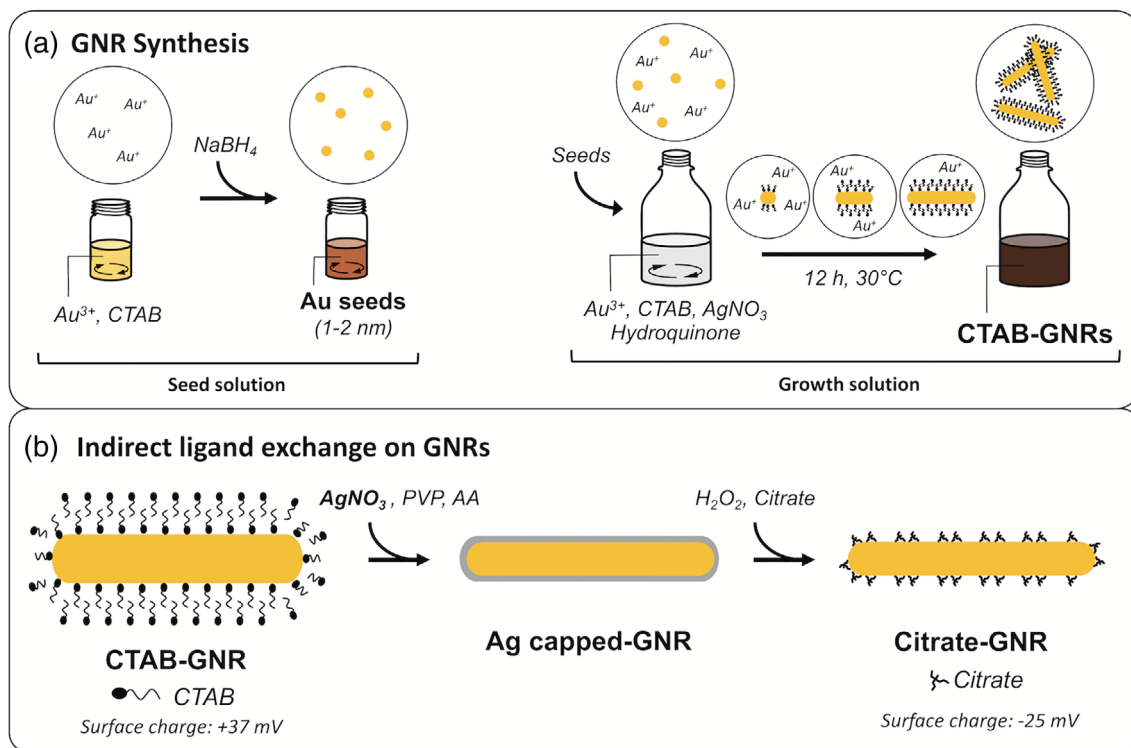


**FIGURE 1** An illustration depicting the synthesis of citrate-capped gold nanorods (GNRs). (A) GNRs were synthesized using a seed-mediated growth method using hydroquinone as a reducing agent for longer aspect ratio, higher purity, and higher yields of GNRs than the ascorbic-acid based synthesis. The seed solution was made by quick addition of ice-cold sodium borohydride ( $\text{NaBH}_4$ ) to a solution of gold chloride and hexadecyltrimethylammonium bromide (CTAB). A small amount of seed solution was added to the growth solution, which contained gold chloride, CTAB, silver nitrate ( $\text{AgNO}_3$ ), and hydroquinone. The solution was left for 12 h in a 30°C water bath for GNRs to grow. (B) The toxic CTAB on CTAB-GNRs were replaced with nontoxic citrate through an indirect ligand exchange protocol. Silver nitrate was used to coat GNRs and displace the CTAB, followed by the etching away of the silver with hydrogen peroxide ( $\text{H}_2\text{O}_2$ ) in a sodium citrate solution. GNRs were left in sodium citrate to generate citrate-GNRs

Burlington, Massachusetts), centrifuged (13,500×g, 20 min), and re-suspended in nanopure water (6 ml).

## 2.4 | GNR characterization

UV-Vis-NIR samples were prepared by diluting centrifuged GNRs in nanopure water (~1:10 ratio GNRs to water) to bring samples into the concentration range of the instrument. UV-Vis-NIR spectra were collected in quartz cuvettes and scanned from 300 to 1300 nm on an Agilent Cary 5000 UV-Vis-NIR spectrophotometer (Agilent, Santa Clara, California) after collecting a baseline using nanopure water.

Surface charge of GNRs (at pH 6.0–6.5) was determined with zeta potential measurements with a Malvern ZetaSizer (Malvern Panalytical, Malvern, UK) in a folded capillary zeta cell (DTS1070, Malvern Panalytical). Samples for zeta potential of CTAB-GNRs were taken directly after the second centrifugation from a 200 ml batch of GNRs that was resuspended in 100 ml of nanopure water (no dilution). Samples of citrate-GNRs were taken after the final centrifugation of the indirect ligand exchange (no dilution).

Surface charge of GNRs was further confirmed with gel electrophoresis using a VWR Gel Electrophoresis System (VWR). Agarose (0.5 w/v% in ×0.5 Tris-Borate-EDTA [TBE] buffer [Fisher, Waltham, Massachusetts]) was dissolved in a microwave (2 min), cooled, and poured into a gel tray with a comb in a casting apparatus (1 h). The resulting gel was run in a gel box filled with TBE buffer (×0.5) at 50 V for 1 h. Samples of CTAB-GNRs or citrate-GNRs (10 µl) were mixed with 2 µl Ficoll 400 (0.15 g/ml in water) to keep the samples in the wells, with 10 µl of sample loaded into each well.

TEM samples were prepared by drying 2 µl of GNRs onto copper grids (Carbon Type-B 300 mesh Copper; Ted Pella Inc., Redding, California) that were plasma-treated (Harrick Basic Plasma Cleaner, 45 s at medium). TEM images were taken by a 200-kV field emission JEOL2010F analytical TEM (JEOL-USA, Peabody, Massachusetts) equipped with a Direct Electron DE-12 camera. ImageJ software (National Institutes of Health, Bethesda, Maryland) was used to determine the length and width from ~250 GNRs from the collected TEM images. The aspect ratio was calculated from these images by dividing the rod length by the width.

Elemental analysis measurements for total gold content and nanorod mass quantification were performed using a NexION2000 Inductively Coupled Plasma-Mass Spectrometer (ICP-MS) (Perkin Elmer, Waltham, Massachusetts) fitted with a High Efficiency Sample Introduction System, as previously described.<sup>18,19</sup> From a 200 ml batch resuspended in 3 ml of nanopure water, batch ICP-MS samples were prepared by dissolving 10 µl of GNRs into 1 ml of aqua regia (3:1 v/v HCl:HNO<sub>3</sub>) for 5 min. The GNRs in aqua regia were further diluted in nanopure water (final dilution ranging from 5 × 10<sup>4</sup> to 2.5 × 10<sup>6</sup>-fold diluted) to obtain a concentration in range of the instrument and prepared standard curves. Single-particle ICP-MS (SP-ICP-MS) samples were prepared using a 5 × 10<sup>6</sup>-fold dilution into nanopure water. For additional details, see the Data S1.

## 2.5 | Pentenoate-functionalized hyaluronic acid (PHA) and gelatin (PGel) synthesis

All materials were purchased from Sigma Aldrich unless otherwise noted. PHA was synthesized from hyaluronic acid (HA, actual MW: 1.56 MDa; Lifecore Biomedical, Chaska, Minnesota) as we previously described.<sup>16</sup> PGel was synthesized using an adapted PHA synthesis protocol and was made from gelatin from porcine skin (Type A, ~300 g Bloom). Briefly, HA (2 g) or gelatin (5 g) were reacted with 4-pentenoic anhydride (2.4 ml per g) in a solution of deionized (DI) water (150 ml for HA or 100 ml for gelatin), 4-(dimethylamino) pyridine (500 mg for HA or 250 mg for gelatin), and N,N-dimethylformamide (200 ml for HA or 50 ml for gelatin). The pH was maintained between 8 and 9 with sodium hydroxide (~1 h) and reacted overnight at room temperature. Sodium chloride (10 g) was added to the PHA reaction. Both reactions were precipitated in acetone (4–8 times the reaction volume), centrifuged (6000×g, 3 min) to collect the pellets, and dissolved in DI water. The pH was adjusted to 7.4 before dialysis (48 h, MWCO: 6–8 kDa, VWR) and lyophilization. PHA and PGel functionalization were determined using Nuclear Magnetic Resonance (NMR) Spectroscopy using a Varian VNMRS-500 MHz NMR Spectrometer equipped with a 5 mm indirect detection room temperature probe (Varian, Palo Alto, California), as described previously.<sup>16</sup> PHA and PGel had 0.59 or 2.06 mmol of pentenoate groups per grams of material, respectively. For additional synthesis and NMR characterization details, see the Data S1.

## 2.6 | Hydrogel crosslinking

Four types of hydrogels were used in the current study for in vitro studies: (1) PGel, (2) PHA, (3) PHA/PGel, and (4) PHA/PGel/GNRs (varying concentrations, indicated in each methods section). Dry PHA and PGel were sterilized using ethylene oxide gas (AN74i, Anderson Anprolene, Haw River, North Carolina) for in vitro studies. PHA/PGel hydrogels consisted of PHA (4 wt%, 40 mg/ml), PGel (5 wt%, 50 mg/ml), photoinitiator Irgacure 2959 (I2959, 0.05 w/v%), crosslinker dithiothreitol (DTT, 2.72 mg/ml), GNRs (varying concentrations, indicated in each methods subsection below), and nanopure water. For additional details, see the Data S1. Hydrogels for all characterization and in vitro studies (see illustration in Figure 2) were formed in a rubber mold (1 mm thickness) between two glass slides and were UV-crosslinked with a handheld 312 nm light at 9 mW/cm<sup>2</sup> (EB-160C, Spectrolite, Westbury, New York) for 2 min on each side. Hydrogels were swollen overnight at 37°C in nanopure water. A 6 mm biopsy punch was used to punch out cylindrical hydrogels.

## 2.7 | Hydrogel conductivity

For electrical conductivity testing, different concentrations of citrate-GNRs (i.e., 0, 0.4, 0.6, 0.8, 1.0, and 1.2 mg/ml) were incorporated into PHA/PGel hydrogels (*n* = 5 or 6). Given the sodium counterion on the

PHA, PHA/PGel hydrogels with no gold were included as baseline controls. Hydrogel resistance (in a hydrated state) was measured using the two-probe method with a 34401A Agilent Multimeter (Agilent, Santa Clara, California) as adapted from previous methods.<sup>20</sup> For additional details regarding the testing setup, see the Data S1. Prior to testing, the heights and diameters of the hydrogels were measured with a micrometer. The conductivity was calculated as the inverse of the resistivity, which was the cross-sectional area multiplied by the resistance and divided by the length (i.e., height of the gel).

## 2.8 | Hydrogel stiffness and swelling

The compressive elastic moduli of PHA/PGel hydrogels with (0.8 mg/ml) and without citrate-GNRs ( $n = 5$  or  $6$ ) were assessed with 8 mm parallel plates on a Discovery Hybrid Rheometer-2 (TA Instruments, New Castle, Delaware) using a strain rate of  $5 \mu\text{m/s}$  ( $\sim 0.25\%$  strain/s) until 20% strain, at  $25^\circ\text{C}$  (under dry conditions), as previously described.<sup>21</sup> Prior to testing, a 0.1 N tare load was applied to hydrogels to ensure the geometry was in contact with the hydrogel and determine the hydrogel height. Hydrogel diameters were measured on a micrometer prior to testing. The compressive elastic modulus was calculated in a custom MATLAB script as the slope of the linear portion of the stress-strain curve (i.e., 5–15% strain).

For absorption and swelling measurements, PHA/PGel hydrogels with (0.8 mg/ml) and without citrate-GNRs were tested ( $n = 6$ ). After hydrogels were formed, each hydrogel was weighed to obtain the fabricated mass. The swollen mass was measured after swelling in

nanopure water (24 h,  $37^\circ\text{C}$ ), and the dry mass was measured after freezing ( $-20^\circ\text{C}$ ) and lyophilization. The swelling ratio was the ratio of the swollen mass to the dry mass. The absorption was the ratio of the swollen mass to the fabricated mass.

## 2.9 | Precursor rheology

For rheological characterization, the viscosity ( $n = 3$ ), yield stress ( $n = 3$ ), and storage modulus recovery ( $n = 3$ ) were measured on a DHR-2 rheometer equipped with parallel 20-mm crosshatched plates (all tests run at  $25^\circ\text{C}$  with a  $500 \mu\text{m}$  gap), as previously described.<sup>16</sup> Briefly, viscosity curves were evaluated using a logarithmic shear rate sweep ( $0.1$ – $100 \text{ s}^{-1}$ ). The yield stress was determined from the cross-over point of the storage ( $G'$ ) and loss ( $G''$ ) moduli from an oscillatory shear stress sweep (1–1000 Pa). The storage modulus recovery was evaluated with three phases of oscillatory shearing (1 Hz) after a 5-min soak time: 5 min of 10 Pa (initial storage modulus), 30 s of 1000 Pa, and 5 min of 10 Pa (recovered storage modulus). The storage modulus recovery was the recovered storage modulus divided by the initial storage modulus and multiplied by 100%.

## 2.10 | Precursor printability assessments

The strut size and pore area of the PHA/PGel/GNR hydrogel precursor was assessed ( $n = 3$ ) by bioprinting with an Inkredible+ bioprinter (Cellink, Gothenburg, Sweden) as we previously described.<sup>16</sup> The

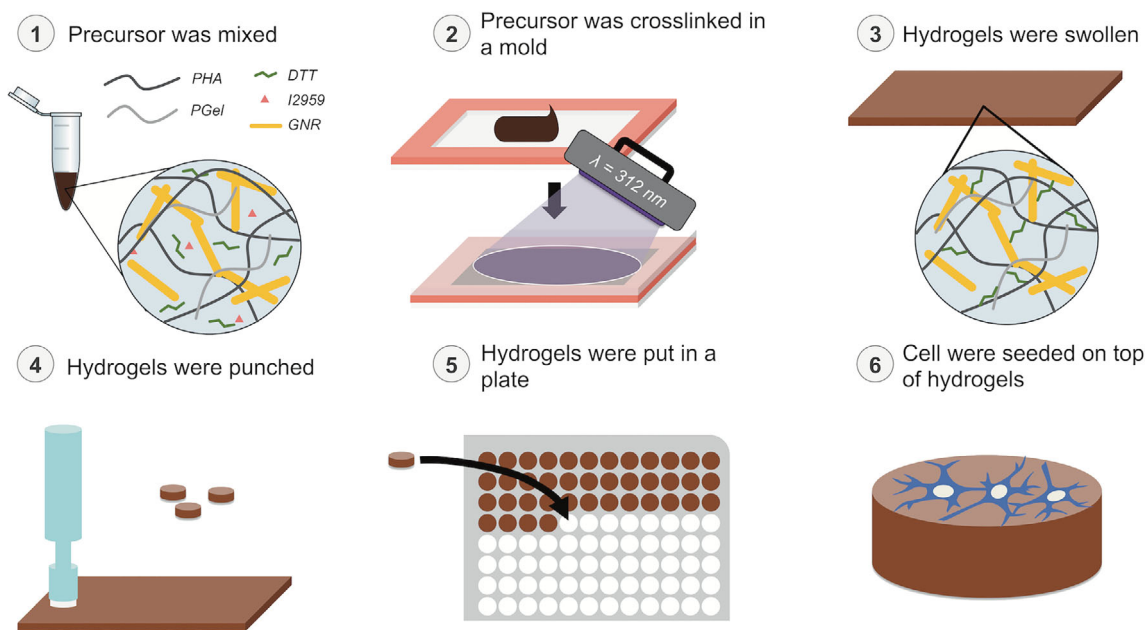


**FIGURE 2** An illustration depicting gold nanorod (GNR) hydrogel formation for in vitro studies. (1) Hydrogel precursor was mixed and contained pentenoate-functionalized hyaluronic acid (PHA), pentenoate-functionalized gelatin (PGel), crosslinker dithiothreitol (DTT), photoinitiator Irgacure 2959 (I2959), and citrate-GNRs. (2) The hydrogel precursor was placed in a rubber gasket mold between two glass slides, followed by UV crosslinking at 312 nm for 2 min on each side. (3) Hydrogels were removed from the molds and swollen in nanopure water overnight at  $37^\circ\text{C}$ . (4) Cylindrical hydrogels were punched using a 6-mm biopsy punch. (5) Hydrogels were placed in a 96-well plate. (6) Rat neural stem cells (rNSCs) were seeded on top of hydrogels and cultured for 7 days

hydrogel precursor was printed into a 3-layer square grid, ( $10 \times 10 \times 0.81$  mm) using printing parameters listed in Table 1. Scaffolds were imaged on a Nikon D5500 camera (Tokyo, Japan) with a Nikon AF-S Micro-NIKKOR 60 mm f/2.8G ED Lens. The strut sizes and pore areas of the bioprinted constructs were analyzed with ImageJ software. The average strut size from each printed sample was determined from the widths of at least 18 different points along the horizontal and vertical struts. The average pore area from each print was determined using the Analyze Particle feature to measure and average the area of the 25 interior pores.

The filament collapse test was performed on PHA/PGel and the GNR hydrogel precursors ( $n = 3$ ) based on previous studies by Therriault et al.<sup>22</sup> and Ribeiro et al.<sup>23</sup> and involved measuring the deflection angle of a printed filament suspended between pillars of varying gap distances (i.e., 1, 2, 4, 8, and 16 mm). A modified platform ( $43.6 \times 4.2 \times 6$  mm,  $L \times W \times H$ ) with the varied gap distances (original CAD file<sup>23</sup>) was printed on a Photon resin printer (Anycubic, Shenzhen, China) using white 3D printing UV sensitive resin (Anycubic). A BioAssemblyBot (Advanced Solutions, Louisville, Kentucky) was used to print a 54 mm line across the top of the pillars (extended 10 mm past the end of the last pillar), while recording with a Nikon D5500 camera. The printing parameters are listed in Table 1. The videos were analyzed 20 s after the print completed (when the filament stopped moving), and the deflection angle was quantified using ImageJ software. The angle was plotted against the gap distance.

A modified filament fusion test was performed on the PHA/PGel and GNR hydrogel precursors ( $n = 3$ ) based on previous studies by Ribeiro et al.<sup>23</sup> A modified print consisted of a 1-layer, back-and-forth pattern in the x-y plane ( $48.8 \times 12$  mm) with increasing distance between each filament (i.e., gap distances starting at 0.5 mm and increasing by 0.01 until 1.1 mm). Hydrogel precursors were printed on a BioAssemblyBot and with the same printing parameters as the filament collapse test. Images were acquired on a Nikon D550 camera and used to determine the gap distance where individual filaments could be distinguished.

To demonstrate structural integrity of taller prints, the PHA/PGel and GNR hydrogel precursors ( $n = 3$ ) were printed into 8-layer, square grids ( $9.68 \times 9.68 \times 2.4$  mm) on the BioAssemblyBot using the printing parameters listed in Table 1. Images were acquired using a Nikon D5500 camera.

## 2.11 | Cytotoxicity in vitro studies

For in vitro studies, PHA/PGel hydrogels with different concentrations of sterile citrate-GNRs (i.e., 0, 0.4, 0.6, and 0.8 mg/ml) were formed and seeded with cells ( $n = 4$  or 5) or were used as acellular material controls ( $n = 3$ ). All cell culture supplies were purchased from Thermo Fisher Scientific (Waltham, Massachusetts) unless otherwise stated. Purchased rat neural stem cells (rNSCs, originally isolated from the cortex of male and female Sprague Dawley rats at day 14 of gestation, Thermo Fisher Scientific) were cultured in coated tissue culture flasks (1% CTS CELLstart Substrate in Dulbecco's PBS with calcium and magnesium, 1 h at 37°C). The medium was changed every 2–3 days with KnockOut DMEM/F-12 Basal Medium supplemented with StemPro Neural Stem Cell Serum Free Medium (NSC SFM) Supplement (2%), recombinant human basic fibroblast growth factor (bFGF; 20 ng/ml), recombinant human epidermal growth factor (EGF; 20 ng/ml), GlutaMAX-I supplement (2 mM), and penicillin-streptomycin (Pen/Strep; 1%). StemPro Accutase Cell Dissociation Reagent was used to dissociate cells for passaging (at 80% confluency). For the in vitro study, cells were seeded at 50,000 cells/cm<sup>2</sup> (passage 2, 16,000 cells/gel) and cultured for 7 days with medium changes every other day.

The media from the cell-seeded hydrogels with 0.8 mg/ml GNRs and no GNRs were collected (on days 1, 3, 5, and 7) for ICP-MS quantification of released gold ( $n = 3$ ). Media samples (50  $\mu$ l) were digested in aqua regia (10-fold dilution, 1 h, 60°C water bath) before 50  $\mu$ l was 100-fold diluted in nanopure water and analyzed by batch ICP-MS according to the GNR Characterization methods section. The background from a media-alone sample was subtracted from all the other samples. The theoretical maximum gold content per GNR hydrogel was estimated to be 22.6  $\mu$ g based on the GNR concentration and volume of the hydrogel. The percentage of total gold was estimated by dividing the gold content in the media samples by the theoretical maximum gold content in one hydrogel.

To evaluate cell adhesion and viability on day 1 and day 7, the alamarBlue Cell Viability Reagent (Thermo Fisher Scientific) was used to measure the metabolic activity of rNSCs, according to manufacturer's instructions. The fluorescence (ex: 540 nm, em: 590 nm) was

**TABLE 1** Printing parameters used for each material on the Inkredible+ and the BioAssemblyBot bioprinters

	PHA/PGel (Inkredible+)	PHA/PGel/GNRs (Inkredible+)	PHA/PGel (BioAssemblyBot)	PHA/PGel/GNRs (BioAssemblyBot)
Assessments	Strut size/pore area (3-layer grids, $10 \times 10 \times 0.81$ mm)		Collapse test/fusion test/8-layer grids ( $9.68 \times 9.68 \times 2.4$ mm)/4-layer grids for in vitro study ( $7.5 \times 7.5 \times 0.8$ mm)	
Tip size/style	27 G tapered nozzle	27 G tapered nozzle	22 G tapered nozzle	22 G tapered nozzle
Print speed (mm/s)	10	10	8	8
Start delay (ms)	300	300	150–175	200–225
Pressure (kPa or psi)	60–80 kPa (8.7–11.6 psi)	100–105 kPa (14.5–15.5 psi)	10–11 psi	12–15 psi
Line height (mm)	0.4	0.4	0.3	0.3

measured on a BioTek Cytation 5 plate reader (BioTek, Winooski, Vermont). The fluorescence was normalized to the average fluorescence of the 0 mg/ml GNR hydrogel group for each day. The hydrogels were then digested overnight at 60°C in 150  $\mu$ l of papain solution (125  $\mu$ g/ml papain from papaya latex, 5 mM N-acetyl cysteine, and 5 mM ethylenedinitrilotetraacetic acid disodium salt dihydrate [EDTA] in PBS), and stored at -20°C as previously described.<sup>24</sup> Before testing, samples were thawed, vortexed, and centrifuged (9391 $\times$ g, 5 min) to pellet any polymer. The DNA content in the supernatant was quantified with the Quant-iT PicoGreen dsDNA Assay Kit (Thermo Fisher Scientific), according to manufacturer's instructions. Fluorescence was measured on a BioTek Cytation 5 plate reader (ex: 485 nm, em: 528 nm). The metabolic activity of each sample was normalized to the DNA content by dividing the alamarBlue fluorescence by the total

DNA content (ng), with further normalization to the 0 mg/ml GNR hydrogel group.

## 2.12 | Bioprinted in vitro study

PHA/PGel and GNR hydrogels (0.8 mg/ml GNRs) were bioprinted into a 4-layer grid (7.5  $\times$  7.5  $\times$  0.8 mm) using a BioAssemblyBot (Advanced Solutions) and using the same printing parameters as the printability assessments (Table 1). Hydrogels were crosslinked with 312 nm UV light for 4 min, and then seeded with rNSCs (Passage 3, 20,000 cells/scaffold), and cultured for 7 days with media exchanges every other day. Live/Dead staining ( $n = 3$ ) was performed on day 7 with the LIVE/DEAD Viability/Cytotoxicity Kit for

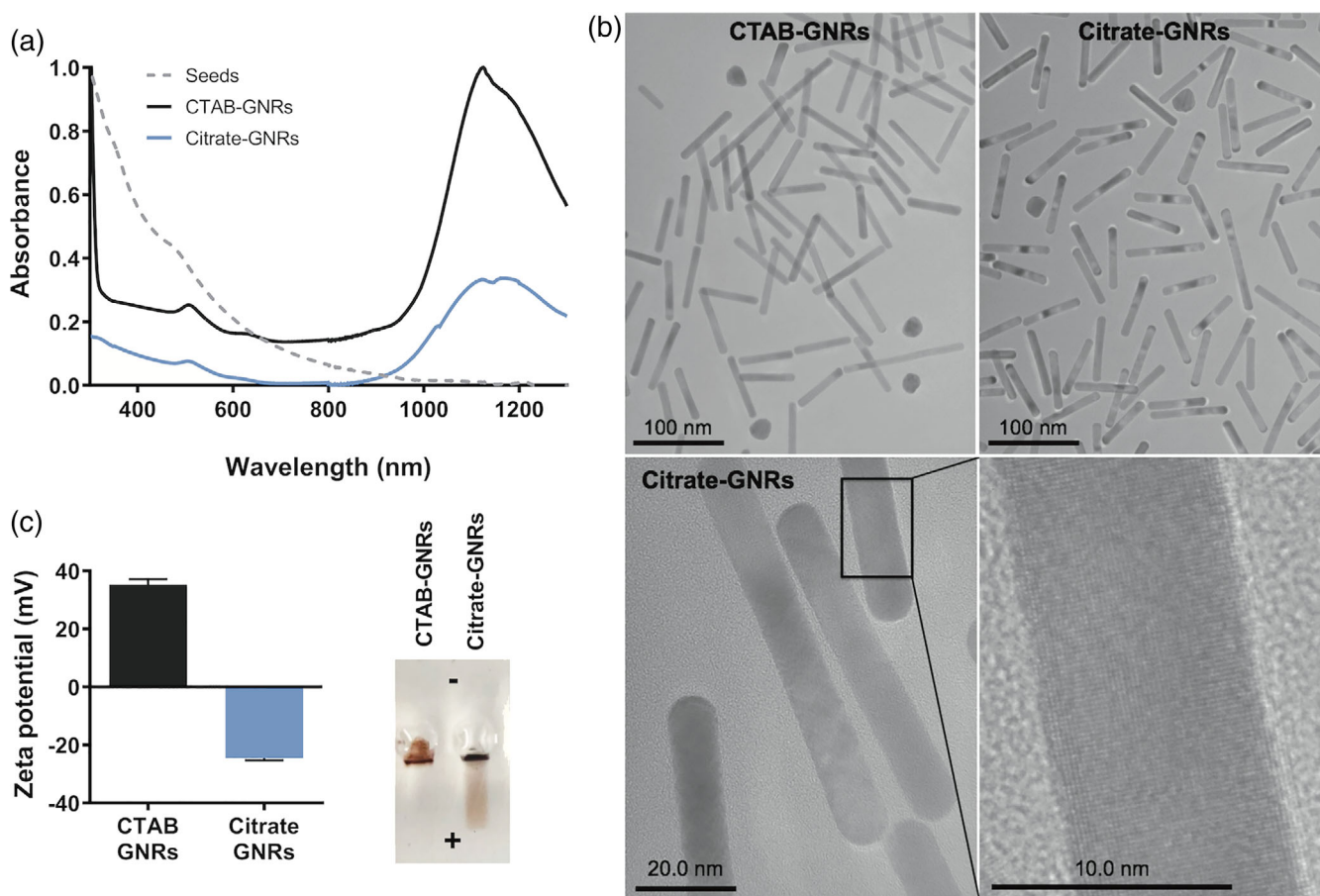


**FIGURE 3** The gold nanorods (GNRs) were characterized to confirm that rods were synthesized and that the hexadecyltrimethylammonium bromide (CTAB) was replaced with citrate on the GNRs during the indirect ligand exchange. (A) The UV-Vis-NIR spectra of the CTAB-GNRs (solid black line), citrate-GNRs (solid lighter blue line), and seed solution (dashed grey line) are shown. The seed solution absorbance was typical of 1–2 nm seeds, and the CTAB- and citrate-GNRs both had typical longitudinal (LSPR) and transverse surface plasmon resonance (TSPR) peaks at 1125 and 507 nm, respectively. (B) The transmission electron microscopy (TEM) images confirmed that GNRs were formed from the synthesis (CTAB-GNRs, upper left panel) with minimal sphere contamination and that the GNRs were retained after the indirect ligand exchange process (citrate-GNRs, upper right panel). Higher magnification of the citrate-GNRs (bottom panels) show a regular rod shape (e.g., no dog-bone shape, or flat caps on the ends) and the atomic lattice structure of gold. (C) The zeta potential (left half) of the CTAB-GNRs was positively charged from the CTAB and the ligand exchange with citrate was confirmed by the change to a negative zeta potential. Additionally, the ligand exchange was confirmed via gel electrophoresis (right half) where the citrate-GNRs migrated toward the cathode and the CTAB-GNRs aggregated and stayed within the well

Mammalian Cells for 30 min (2  $\mu$ M calcein AM, 3 mM ethidium homodimer-1 (Thermo Fisher Scientific). The rNSCs on hydrogels were imaged on a Leica SP8 confocal laser scanning microscope using a  $\times 20$ , 0.75 NA oil objective (Leica Microsystems, Buffalo Grove, Illinois). An argon laser line was used to excite the calcein AM and ethidium homodimer-1, and the live signals were detected with an emission detection window set at 500–550 nm. Meanwhile, the dead signals were detected with an emission window set at 620–740 nm.

For immunostaining ( $n = 3$ ), rNSCs on hydrogels were fixed for 20 min in 10% neutral buffered formalin, rinsed with PBS, and permeabilized in 0.3% TritonX-100 (1 h, room temperature). Hydrogels were blocked in 5% goat serum and 1% bovine serum albumin in PBS-TWEEN (PBST, 0.05% TWEEN 20) overnight at 4°C. Then, hydrogels were incubated with primary antibodies in the blocking solution overnight at 4°C. Primary antibodies to detect neural stem cells and neurons were mouse anti-Nestin (2  $\mu$ g/ml, Fisher 14-5843-82) and rabbit anti-MAP2 (2  $\mu$ g/ml, Abcam ab32454), respectively. Hydrogels were rinsed 3 times in PBST for 5 min each and incubated with secondary antibodies for 2 h at room temperature. The secondary antibodies were goat anti-mouse IgG H&L Alexa Fluor 647 preadsorbed (5  $\mu$ g/ml, Abcam ab150119) and goat anti-rabbit IgG H&L Alexa Fluor 488 (10  $\mu$ g/ml, Abcam ab150077). Hydrogels were rinsed 3 times in PBST (5 min each), before nuclei were stained with DAPI (500 nM) for 1 h at room temperature, and rinsed three times in PBS. The rNSCs

on hydrogels were imaged on a Leica SP8 confocal laser scanning microscope with a  $\times 20$  oil objective. DAPI signals were excited by a 405 nm Diode laser and detected between 415 and 470 nm. Secondary antibodies Alexa Fluor 488 and Alexa Fluor 647 were excited by an argon laser and a HeNe 633 nm laser, respectively, and were detected at 500–550 nm and 650–750 nm, respectively.

For Live/Dead and immunofluorescent staining of each hydrogel, the entire scaffold was first scanned with Tile Scanning. Then, sample regions, normally 12 to 15 tiles, were selected to run the sequential scanning to acquire z-series of images. Tiles were merged with the smooth blended algorithm in the Leica LAS X software. ImageJ software was used to merge the channels.

## 2.13 | Statistical methods

All statistical analyses were performed in GraphPad Prism (GraphPad Software Inc., La Jolla, California). An unpaired t-test was used to compare the CTAB- and citrate-GNR's aspect ratio, length, and width, the yield stress assessment, storage modulus recovery, strut size, pore area, and filament fusion test. A one-way analysis of variance (ANOVA) was used to analyze results from hydrogel conductivity, mechanical, swelling, and absorption testing, metabolic activity, and metabolic activity normalized to DNA content, followed

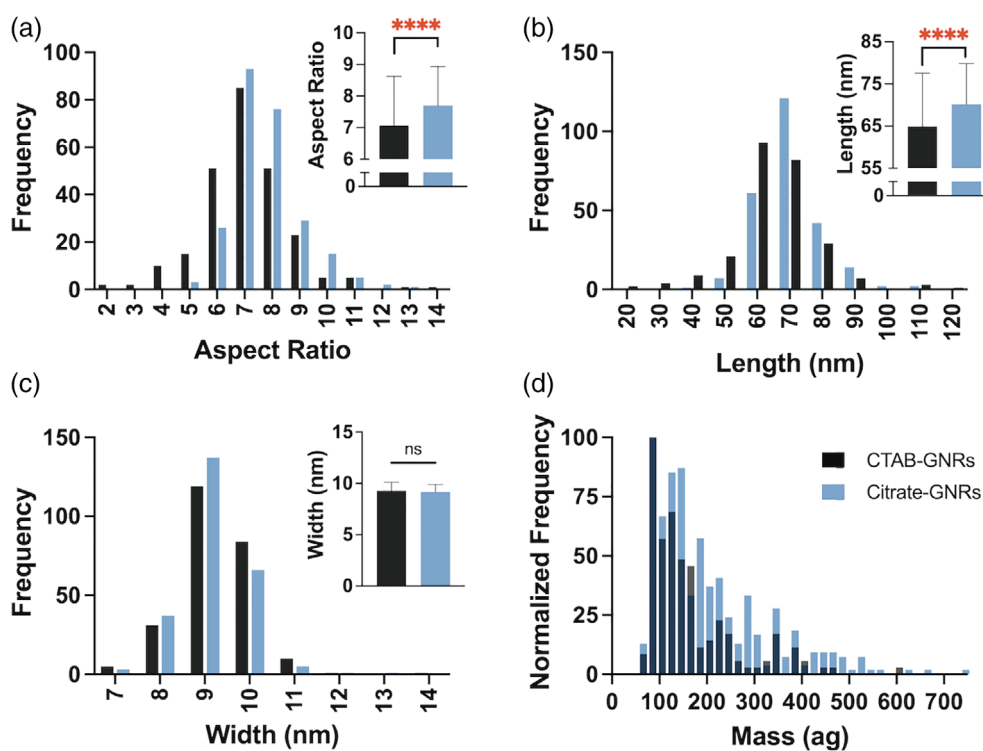


**FIGURE 4** The citrate-GNRs (shown in blue) had high aspect ratios of  $\sim 7$ – $8$  and lengths of  $\sim 70$  nm, which were greater than those of the CTAB-GNRs (shown in black). (A) The histogram of the aspect ratio showed similar distributions between the citrate- and CTAB-GNRs, but the average aspect ratio (shown in the inset) of citrate-GNRs was  $\sim 6\%$  higher than the CTAB-GNRs. (B) The histogram of the lengths showed similar distributions between the citrate- and CTAB-GNRs, but the average length (shown in the inset) of citrate-GNRs was  $\sim 8\%$  longer than the CTAB-GNRs. (C) The histogram and the average widths (shown in the inset) showed similar distributions and widths between the citrate- and CTAB-GNRs. (D) Single-particle ICP-MS showed similar and overlapping mass distributions between citrate- and CTAB-GNRs. \*\*\*\* $p < .0001$



by Tukey's post hoc test. A two-way ANOVA was used to analyze the viscosity curves, filament collapse test, and DNA content. Differences with  $p < .05$  were considered significant. Results were reported as the mean  $\pm$  SD.

### 3 | RESULTS

#### 3.1 | CTAB- and citrate-GNRs characterization

UV-Vis-NIR spectra in Figure 3A of the seed solution and CTAB-GNRs confirmed the formation of gold nanorods with longitudinal (LSPR) and transverse surface plasmon resonance (TSPR) peaks at 1125 and 507 nm, respectively. The TEM images of CTAB-GNRs in Figure 3B further confirmed the formation of nanorods with minimal contamination by spheres. After replacing the CTAB with citrate on GNRs, the UV-Vis-NIR spectrum of citrate-GNRs

(Figure 3A) confirmed that there were nanorods with the same LSPR and TSPR peaks as the CTAB-GNRs. Figure 3B shows a representative TEM image of the citrate-GNRs, which confirmed that GNRs had not changed shape. The replacement of CTAB with citrate was verified by a change in surface charge from  $37 \pm 7$  mV with CTAB-GNRs to  $-25 \pm 8$  mV with citrate-GNRs (Figure 3C), given that CTAB is positively charged and citrate is negatively charged. Gel electrophoresis showed that the citrate-GNRs migrated toward the cathode (Figure 3C) and further verified the negatively charged citrate-GNRs, as compared to the CTAB-GNRs, which stayed in the well.

The aspect ratio, length, and width of the CTAB- and citrate GNRs were determined from ImageJ analyses (Figure 4A-C, respectively), and the mass distributions were determined from SP-ICP-MS (Figure 4D). Citrate-GNRs had  $\sim 6\%$  higher aspect ratios ( $7.7 \pm 1.2$  vs.  $7.1 \pm 1.6$ ,  $p < .0001$ ) and were  $\sim 8\%$  longer ( $70 \pm 10$  nm vs.  $65 \pm 13$  nm,  $p < .0001$ ) than CTAB-GNRs, but did not have significantly

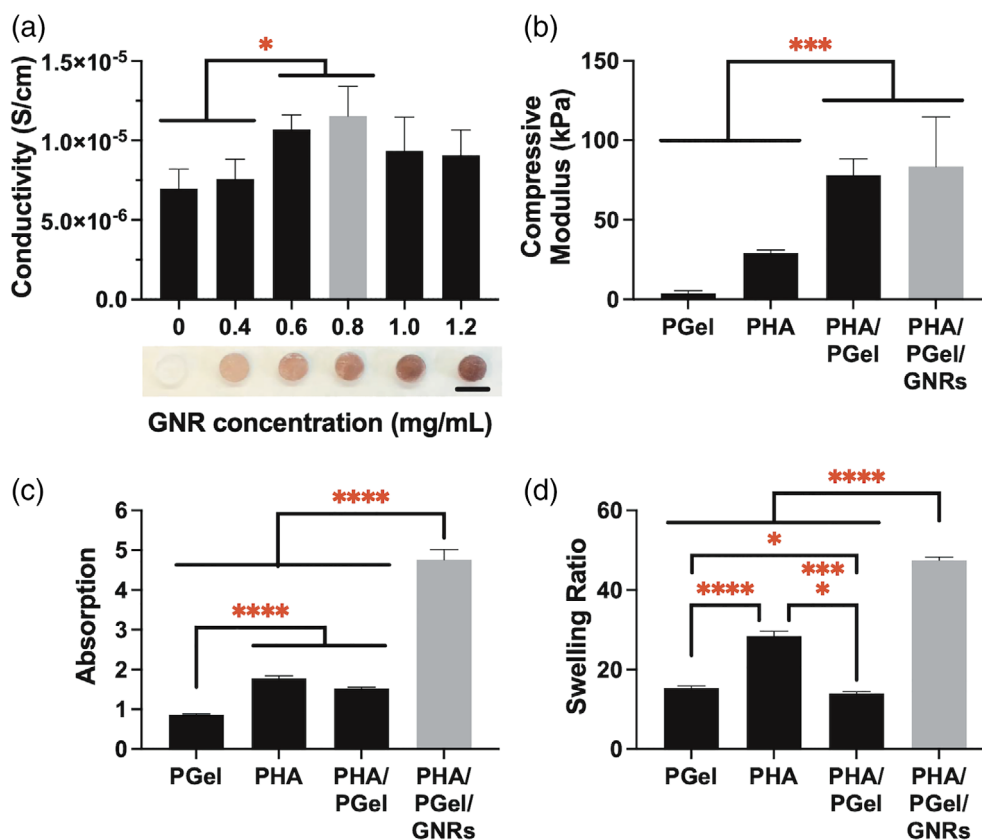


**FIGURE 5** The conductivity of pentenoate-functionalized hyaluronic acid (PHA)/pentenoate-functionalized gelatin (PGel) hydrogels were increased with the addition of 0.6 or 0.8 mg/ml of citrate-coated gold nanorods (citrate-GNRs). (A) The conductivity of the GNR hydrogels (hydrated) was measured with citrate-GNR concentrations ranging from 0 to 1.2 mg/ml ( $n = 5$  or  $6$ ), with the most conductive formulations containing 0.6 and 0.8 mg/ml GNRs. Coloration of the gels after swelling is shown below the respective concentration on the x-axis. Scale bar: 6 mm. (B) The compressive elastic modulus of the GNR hydrogels were not significantly different that of the PHA/PGel hydrogels ( $n = 5$  or  $6$ ), but both were greater than the PHA and PGel hydrogels alone. (C) The GNR hydrogels absorbed more water after fabrication than the PHA/PGel, PHA, and PGel hydrogels ( $n = 6$ ). The PHA and PHA/PGel had similar absorption to each other and both absorbed more than PGel, which actually lost water after fabrication. (D) The swelling ratio of the GNR hydrogels was greater than that of PHA/PGel, PHA, and PGel hydrogels ( $n = 6$ ). The PHA had a greater swelling ratio than that of the PHA/PGel and gelatin hydrogels. The PHA/PGel had a greater swelling ratio than that of the PGel hydrogels. \*  $p < .05$ , \*\*\*  $p < .001$ , \*\*\*\*  $p < .0001$

different widths ( $9.2 \pm 0.7$  vs.  $9.3 \pm 0.8$  nm). Single-particle ICP-MS showed that CTAB- and citrate-GNRs had similar mass distributions with overlapping mass histograms.

Batch ICP-MS was used to measure the total gold content of the CTAB-GNRs and citrate-GNRs. The synthesis had an ~80%

yield, and after replacing the CTAB with citrate and sterile-filtering, there was a ~29% yield for that step. The yield was further confirmed by the three-fold decrease in absorbance of the UV-Vis-NIR spectrum for citrate-GNRs compared to the CTAB-GNRs ( $\lambda_{\text{LSPR}} = 1.00$  vs. 0.33).

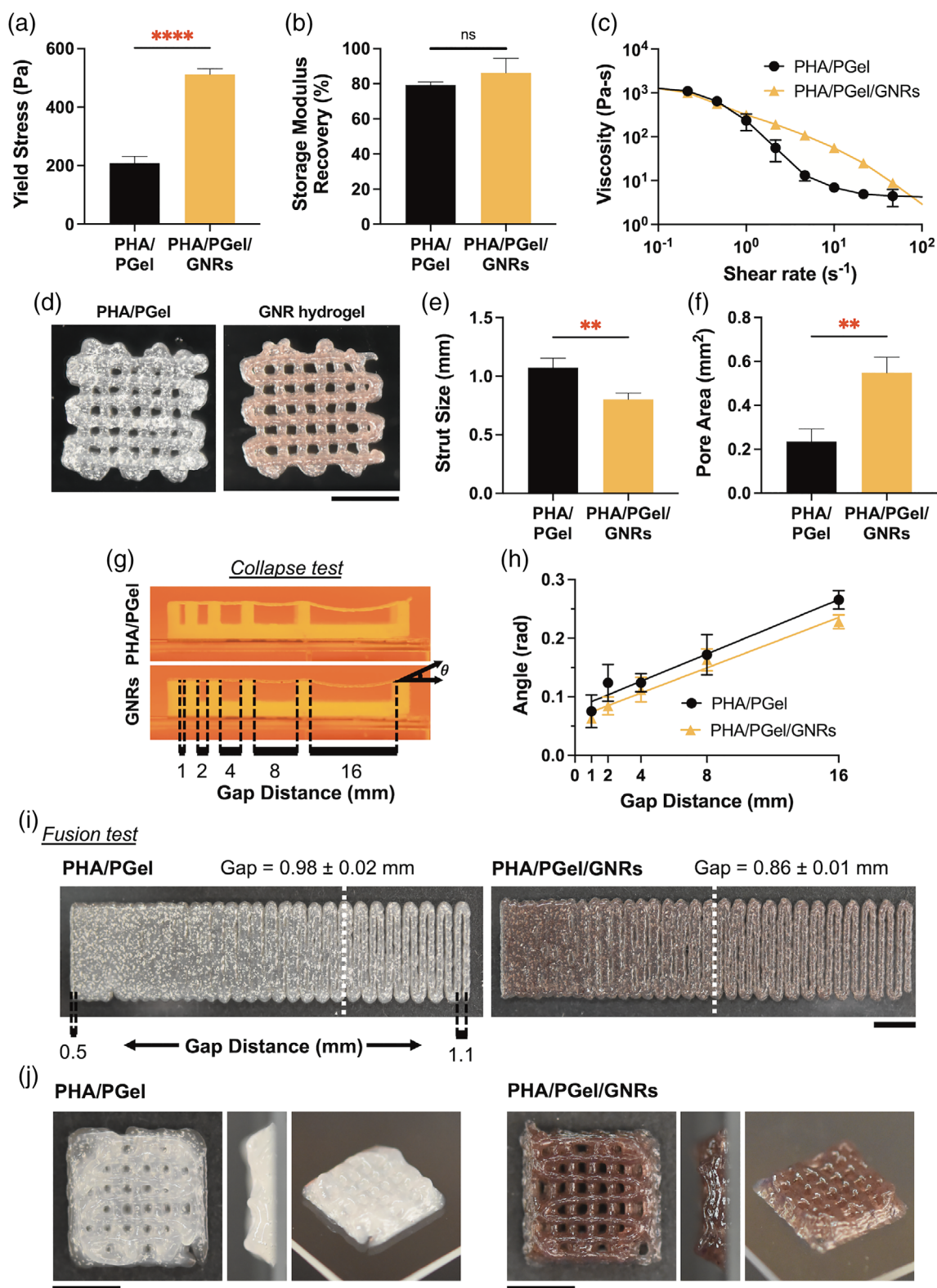
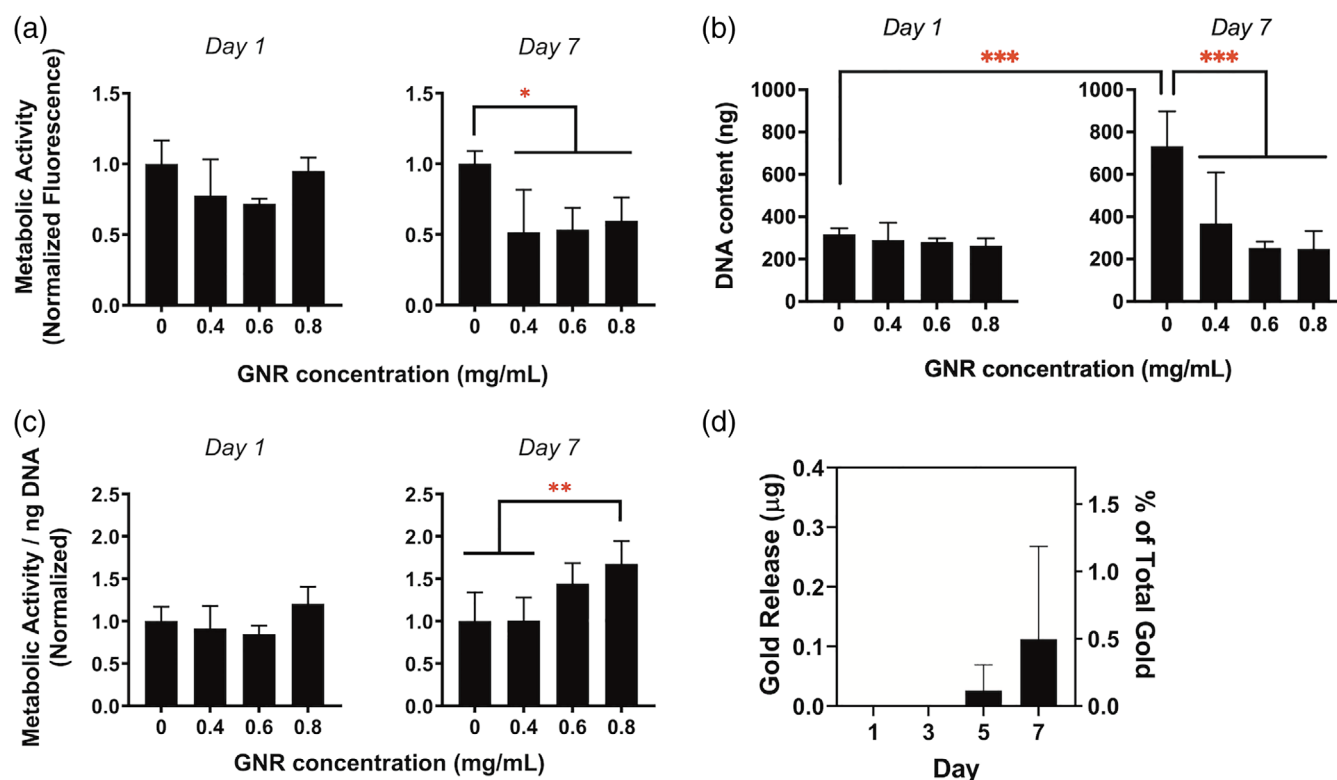


FIGURE 6 Legend on next page.

### 3.2 | Hydrogel conductivity

The conductivity of the PHA/PGel/GNR hydrogels (or GNR hydrogels) were determined with varied amounts of GNRs (i.e., 0, 0.4, 0.6,

0.8, 1.0, and 1.2 mg/ml), where the conductivity increased along with increasing GNR content up to 0.8 mg/ml GNRs (Figure 5A). The 0.8 mg/ml GNR hydrogel group ( $1.15 \times 10^{-5} \pm 0.19 \times 10^{-5}$  S/cm) had 71% and 58% higher conductivity than that of the 0 and



**FIGURE 7** In vitro assessment of seeded rat neural stem cells (rNSCs) on gold nanorod (GNR) hydrogels showed the hydrogels were not cytotoxic for rNSCs and < 1% of the total gold was released in the media samples during the 7 days of culture. (A) The total metabolic activity of seeded rNSCs on day 1 was not significantly across that of different pentenoate-functionalized hyaluronic acid (PHA)/pentenoate-functionalized gelatin (PGel) hydrogels, but was decreased after 7 days ( $n = 4$  or  $5$ ). (B) The total DNA content was not significantly across between any groups on day 1 but was higher in the hydrogels with no GNRs on day 7 compared to the hydrogels with 0.4 to 0.8 mg/ml of GNRs ( $n = 4$  or  $5$ ). (C) The normalized metabolic activity per nanogram of DNA and to the hydrogel with no GNRs was not significantly across any of the groups on day 1; however, on Day 7, the hydrogels with 0.8 mg/ml of GNRs had 1.7 times greater metabolic activity than that of the hydrogels with 0 or 0.4 mg/ml GNRs. (D) The media samples from the hydrogels with 0.8 mg/ml of GNRs and cells had  $0.026 \pm 0.043 \mu\text{g}$  of gold (or  $\sim 0.12\%$  of the total gold in a hydrogel) in the day 5 media samples, and  $0.11 \pm 0.16 \mu\text{g}$  ( $\sim 0.49\%$  of the total gold) in the day 7 samples ( $n = 3$ ) (left y-axis). Compared to the maximum gold content per GNR hydrogel, there was less than 1% of the gold released over 7 days of culture (right axis). The medium samples from the hydrogels with no gold did not have an amount of gold that was above the background. \* $p < .05$ , \*\* $p < .01$ , \*\*\* $p < .001$

**FIGURE 6** Rheological characterization of gold nanorod (GNR) hydrogel precursors showed similar shear thinning, higher yield stress, similar storage modulus recovery, and better printability than pentenoate-functionalized hyaluronic acid (PHA)/pentenoate-functionalized gelatin (PGel) alone. (A) The viscosity curves of PHA/PGel/GNR (GNR hydrogel) precursors were not significantly different over different shear rates, and both were shear thinning ( $n = 3$ ). (B) The yield stress of GNR hydrogel precursors was 2.4 times higher than that of the PHA/PGel precursors ( $n = 3$ ). (C) The storage modulus recovery (5 s postshearing) was not significantly different from that of the PHA/PGel precursors ( $n = 3$ ). (D) A 3-layer, square grid ( $10 \times 10 \times 0.81 \text{ mm}$ ) was bioprinted for assessing pore area and strut size. (E) The bioprinted PHA/PGel precursors had 34% greater printed strut sizes compared to GNR precursors ( $p < .01$ ). (F) The GNR precursors had 2.3 times larger pore areas ( $p < .01$ ), and overall better printability. (G) For the filament collapse test, a single strut was printed across pillars with gaps of various distances (i.e., 1, 2, 4, 8, and 16 mm). (H) The angle of deflection ( $\theta$ ) was measured 20 s after each print was completed, and the bioprinted PHA/PGel precursor had a 17% greater angle than that of the bioprinted GNR precursor ( $n = 3$ ,  $p < .05$ ). (I) The filament fusion test was a series of printed struts in the x-y plane with increasing distance between the struts in the x direction (i.e., from 0.5 to 1.1 mm gap distances). For each print, the smallest gap distance where individual struts were unfused and could be distinguished was designated the gap distance where fusion occurs (indicated by a dotted white line). The PHA/PGel precursor fused at a gap distance that was 13% greater than that of the GNR precursor ( $n = 3$ ,  $p < .001$ ), indicating better printability of the GNR precursor. (J) To show structural stability, 8-layer, square grid scaffolds ( $9.68 \times 9.68 \times 2.4 \text{ mm}$ ) were bioprinted for PHA/PGel and the GNR precursor (top view (left), side view (middle), isometric view (right)). The GNR precursor held the scaffold shape better than the PHA/PGel scaffold. All scale bars: 5 mm. \*\*\*\* $p < .0001$

0.4 mg/ml groups ( $p < .01$ ), respectively. The conductivity of the 0.6 mg/ml GNR hydrogel group ( $1.07 \times 10^{-5} \pm 0.09 \times 10^{-5}$  S/cm) was 57% and 44% higher than that of the 0 and 0.4 mg/ml groups ( $p < .05$ ), respectively. The conductivity of the 1.0 and 1.2 mg/ml GNR hydrogels were not significantly different from any other group, therefore, the 0 to 0.8 mg/ml concentrations proceeded forward to be tested in vitro.

### 3.3 | Hydrogel stiffness and swelling

The compressive elastic moduli, absorption, and swelling ratio of the most conductive GNR hydrogel (i.e., 0.8 mg/ml GNRs) were compared to PHA/PGel, PHA, and PGel hydrogels (Figure 5B–D, respectively). As shown in Figure 5B, the compressive elastic moduli of the GNR hydrogels were not significantly different from the moduli of PHA/PGel hydrogels ( $83 \pm 30$  kPa and  $78 \pm 10$  kPa, respectively). Compared to PHA or PGel hydrogels alone, the GNR hydrogels were 2.9 times stiffer than PHA hydrogels ( $29 \pm 2$  kPa,  $p < .0001$ ) and 21 times stiffer than PGel hydrogels ( $4 \pm 2$  kPa,  $p < .0001$ ). Similarly, PHA/PGel hydrogels were 2.7 and 20 times stiffer than PHA hydrogels ( $p < 0.001$ ) and PGel hydrogels ( $p < .0001$ ), respectively.

As shown in Figure 5C, the water absorption of the GNR hydrogels was 2.7, 3.2, and 5.6 times greater ( $p < .0001$ ) than PHA, PHA/PGel, and PGel hydrogels, respectively. PHA and PHA/PGel hydrogel absorptions were 2.1 and 1.8 times greater ( $p < .0001$ ) than those of PGel hydrogels, respectively. Similar trends were observed for swelling in Figure 5D, where the swelling ratios of GNR hydrogels were 1.7, 3.1, and 3.4 times greater ( $p < .0001$ ) than for PHA, PGel, and PHA/PGel, respectively. PHA hydrogels had a swelling ratio that was 1.8 and 2.0 times greater ( $p < .0001$ ) than those of PGel and PHA/PGel, respectively. PGel hydrogels had a swelling ratio 10% greater than those of PHA/PGel ( $p < .05$ ). Overall, the addition of GNRs to PHA/PGel increased the absorption of water from fabrication to the swollen state, and increased the swelling ratios of the swollen state to the dry state.

### 3.4 | Hydrogel precursor rheology

The viscosity, yield stress, and storage modulus recovery (Figure 6) of the GNR hydrogel precursor (labeled as PHA/PGel/GNRs in Figure 6) are shown compared to the PHA/PGel precursor (with no GNRs). The viscosities (Figure 6A) of GNR hydrogel precursors versus

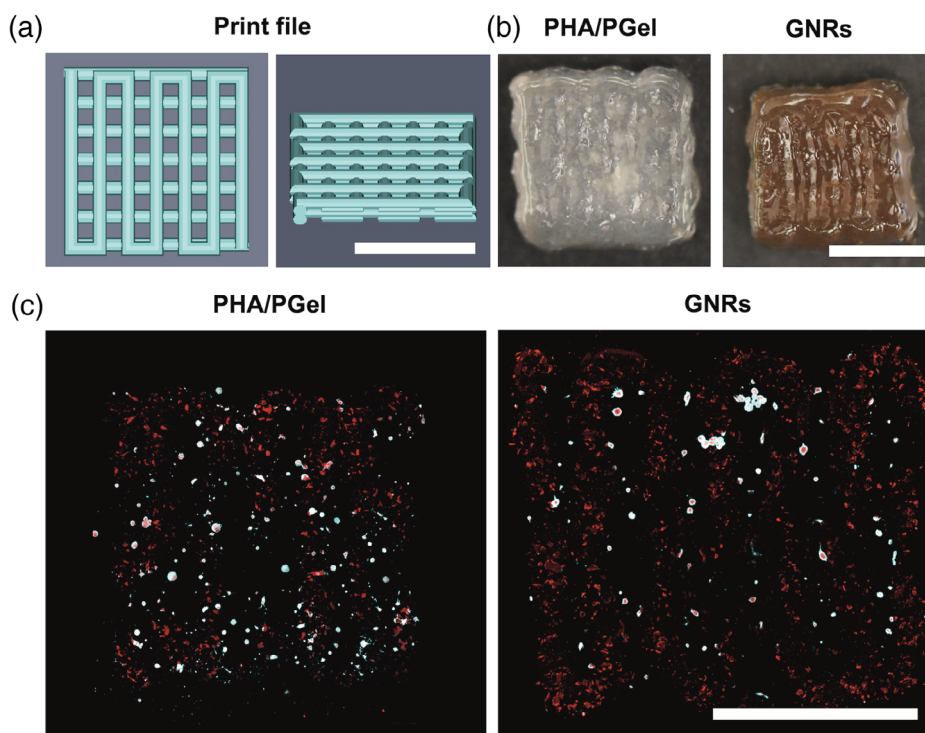


**FIGURE 8** The rat neural stem cells (rNSCs) were seeded on top of bioprinted PHA/PGel and GNR hydrogels, and after 7 days, were distributed homogeneously on the PHA/PGel scaffolds, but were located between the printed struts on the GNR hydrogels. (A) The top and front views of the 4-layer grid print file are shown ( $7.5 \times 7.5 \times 0.8$  mm). (B) PHA/PGel (left) and GNR hydrogels (right) were bioprinted into 4-layer grids, crosslinked, and seeded with rNSCs hydrogels for Live/Dead staining and immunofluorescent staining. The vertical struts are visible and distinguishable from each other, but fused into 1 layer. (C) On Day 7, confocal tile scanning generated overviews of the entire hydrogels to visualize the relative positioning of the cells (nestin staining, false-colored to cyan for visualization) and the bioprinted hydrogel struts (autofluorescent PGel, false-colored to red for visualization). The rNSCs formed spheroids on top of the hydrogel that were adhered homogeneously across surface of the bioprinted PHA/PGel scaffolds; however, the rNSCs formed larger spheroids on the surface of the GNR hydrogel scaffolds, and were distributed between the bioprinted struts. All scale bars: 5 mm

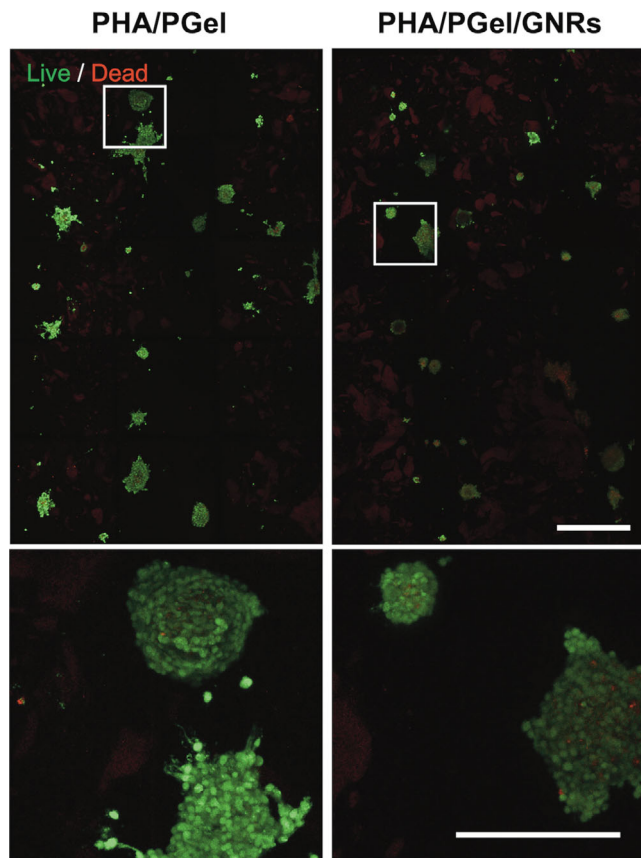


**FIGURE 9** Live/Dead staining of rat neural stem cells (rNSCs) seeded on PHA/PGel (left) and GNR hydrogels (right) for 7 days showed the rNSCs formed spheroids on both hydrogels. Higher magnification images of each hydrogel (bottom) show live spheroids (green) on both hydrogels and few dead cells (red) within the spheroids and some as single dead cells on the hydrogels. The PGel was autofluorescent in the dead channel and was visible as the dimmer red areas (as opposed to stained dead nuclei, which were smaller bright red spots). Scale bar: 500  $\mu\text{m}$ . Inset scale bar: 200  $\mu\text{m}$

the PHA/PGel precursors were not significantly different over the tested shear rates. However, the yield stress (Figure 6B) of the GNR hydrogels precursors ( $511 \pm 20$  Pa) was 2.4 times higher than the PHA/PGel hydrogel precursors. The storage modulus recovery (Figure 6C) of GNR hydrogel precursors ( $86 \pm 8$  Pa) was not significantly different than the PHA/PGel hydrogel precursors.

### 3.5 | Hydrogel precursor printability assessments

The GNR hydrogels precursors that were bioprinted into the 3-layer grids (Figure 6D) had higher printed shape fidelity than the PHA/PGel without GNRs. The strut size (Figure 6E) was 34% greater in the PHA/PGel ( $p < .01$ ), which resulted in the GNR hydrogel precursors having 2.3 times larger pore areas (Figure 6F) ( $p < .01$ ). For the filament collapse test (Figure 6G, H), the PHA/PGel precursor had an overall mean deflection angle ( $\theta$ ) that was 17% greater than that of the GNR precursor ( $p < .05$ ). For the filament fusion test (Figure 6I),

the PHA/PGel precursor fused a gap distance that was 13% greater than that of the GNR precursor ( $p < .001$ ). To demonstrate the structural integrity of taller printed scaffolds, 8-layer grids were bioprinted for PHA/PGel and the GNR precursor, and the GNR hydrogel scaffold showed better building potential and shape fidelity than the PHA/PGel precursor.

### 3.6 | In vitro toxicity of GNR hydrogels with citrate-GNRs to rat neural stem cells

The adhesion and proliferation of rNSCs cultured on GNR hydrogels were analyzed by the total metabolic activity (Figure 7A), DNA content (Figure 7B), and the normalized metabolic activity per ng of DNA (Figure 7C). The total metabolic activity and DNA content of rNSCs on day 1 were not significantly different between the hydrogel groups. On day 7, in general the metabolic activity and DNA content of the hydrogels with no GNRs was higher than the hydrogels with GNRs, but the hydrogels with GNRs had higher metabolic activity when normalized to DNA content. Specifically, the metabolic activity of rNSCs on hydrogels with no GNRs was ~92%, ~89%, and ~67% greater than the 0.4 ( $p < .01$ ), 0.6 ( $p < .01$ ), and 0.8 ( $p < .05$ ) mg/ml GNR hydrogel groups, respectively. Similarly, the total DNA content on day 7 of hydrogels with no GNRs was ~2, ~2.9, and ~2.9  $>$  0.4 ( $p < .001$ ), 0.6 ( $p < .0001$ ), and 0.8 ( $p < .0001$ ) mg/ml GNR hydrogels. Additionally, the hydrogels without GNRs on day 7 had 2.3 times greater DNA content than on day 1 ( $p < .0001$ ). On day 1, the metabolic activity normalized to the DNA content did not show any significant differences between groups; however, on day 7, the 0.8 mg/ml GNR hydrogel had 68% and 45% greater metabolic activity per ng of DNA than 0 and 0.4 mg/ml hydrogel groups, respectively ( $p < .01$ ). While the 0.6 mg/ml GNR hydrogel group had a higher metabolic activity per ng of DNA than 0 and 0.4 mg/ml groups, the increase was not statistically significant.

The medium changes from the GNR hydrogels (0.8 mg/ml of GNRs) with cells were analyzed for released gold by batch ICP-MS (Figure 7D). The amount of gold in the 0 mg/ml GNR hydrogels with cells were not higher than the background (data not shown). The amount of gold released on the first and third day were not higher than the background, but there was  $0.026 \pm 0.043$   $\mu\text{g}$  in the day 5 media samples, and  $0.11 \pm 0.16$   $\mu\text{g}$  in the day 7 samples. One of the three samples did not have an amount of gold higher than the background and caused the large standard deviations. Compared to the theoretical maximum gold content per GNR hydrogel, the day 3 and day 5 media samples had released ~0.12% and ~0.49% of the total gold in the hydrogel, respectively.

### 3.7 | In vitro evaluation of rNSCs on bioprinted GNR scaffolds

PHA/PGel and GNR hydrogels were bioprinted into 4-layer grids with each filament fusing but distinguishable (Figure 8A,B). The confocal tile scanning of immunofluorescent stains generated an

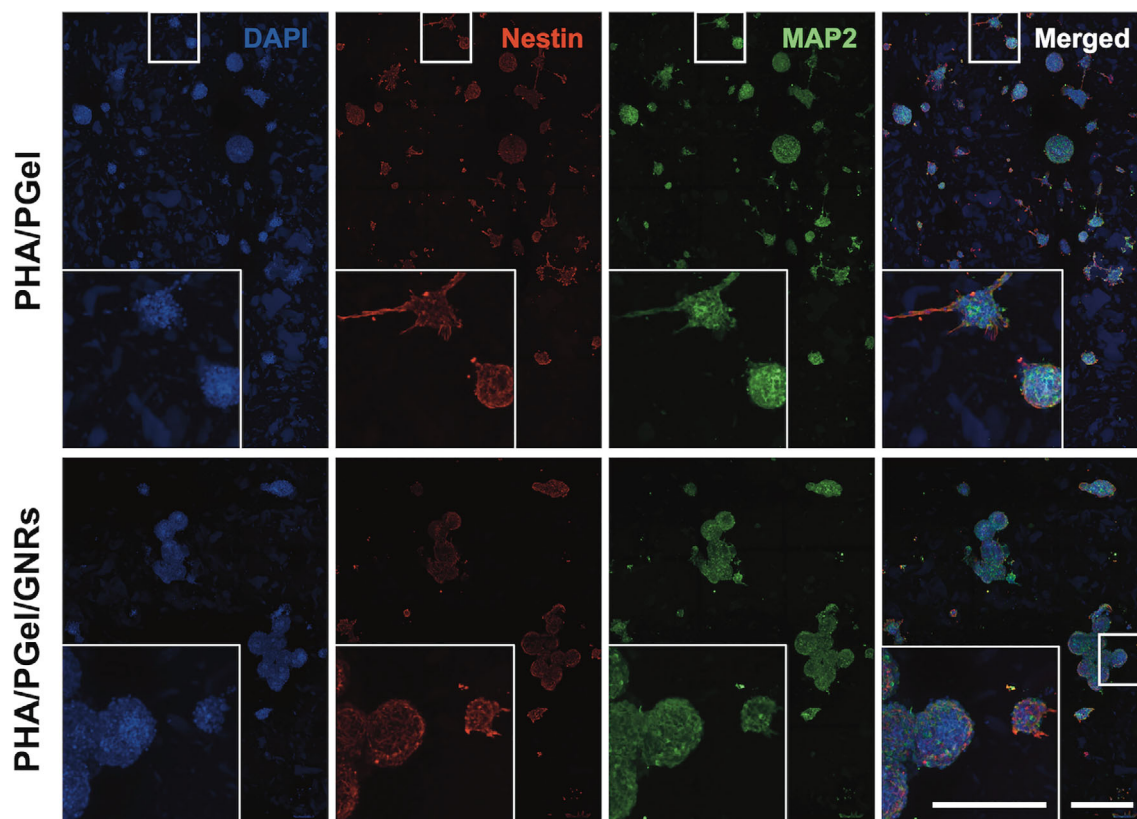


**FIGURE 10** Immunofluorescent staining of rat neural stem cells (rNSCs) seeded on PHA/PGel and GNR scaffolds for 7 days showed positive staining for a neural stem cell marker (nestin, red) and a neural marker (MAP2, green) in both hydrogels. Spheroids on the PHA/PGel hydrogels were adhering and spreading on the hydrogel. Spheroids on the GNR hydrogels were adhering mostly to other spheroids with less spreading on the hydrogel in general. On both hydrogels, nestin staining was brighter on the exterior of the spheroids, while MAP2 staining was brighter on the interior of the spheroids. The PGel was autofluorescent in the DAPI channel and was visible as the dimmer blue areas (as opposed to the brighter stained nuclei). All scale bars: 500  $\mu$ m

overview of the entire hydrogel (Figure 8C) for visualizing the relative positions of hydrogel (autofluorescent PGel in the DAPI channel, false-colored red), and the rNSC spheroids (nestin staining, false-colored cyan) after 7 days. The rNSCs formed spheroids on top of both hydrogels and were adhered homogeneously across the PHA/PGel hydrogels; however, on the GNR hydrogels, the spheroids were located between the printed struts and formed larger spheroids that tended to clump together.

Live/Dead staining after 7 days showed viable rNSC spheroids on top of both hydrogels with live cells and few dead cells (Figure 9). Higher magnification showed the distribution of several live (green) and few dead (red) cells within the spheroids and a few singled out dead cells on each hydrogel. The PGel was autofluorescent (in the dead channel) and were the dimmer red spots.

Immunofluorescent staining after 7 days (Figure 10) showed that rNSCs on both PHA/PGel and GNR hydrogels stained positive for the neural stem cell marker (nestin, red) and a neuron marker (MAP2, green). However, there were not qualitative differences in the intensity or distribution of nestin and MAP2 between rNSCs on PHA/PGel and GNR hydrogels. The most noticeable difference was that rNSC spheroids on the PHA/PGel hydrogels had adhered and spread more

on the hydrogel, specifically on the PGel patches, which were visible from PGel autofluorescence in the DAPI channel, dimmer/larger blue areas compared to brighter/smaller nuclei staining. On the other hand, spheroids on the GNR hydrogels maintained a more spherical morphology and had adhered to other spheroids with less spreading on the hydrogel in general. On both hydrogels, nestin staining was brighter on the exterior of the spheroids, while MAP2 staining was brighter on the interior of the spheroids (see Figure 10 higher magnification insets).

## 4 | DISCUSSION

We developed and fully characterized a new conductive GNR hydrogel with an injectable and paste-like precursor capable of rapidly crosslinking, to enable easier surgical application in a rat SCI model. The developed PHA/PGel/GNR bioink provides a translational biomaterial platform for future application to SCI that was (1) conductive once crosslinked, (2) noncytotoxic, and (3) possessed an injectable and paste-like precursor for easier surgical translation. The GNR hydrogel provides a translational conductive biomaterial platform and starting

point for further refinement and eventual combination with ES to promote axon regeneration, neural plasticity/reorganization, and functional recovery.

There are several limitations of GNRs that may hinder the development of conductive biomaterials for biomedical applications that were overcome: challenges in the synthesis, low aspect ratios, low synthesis yields, cytotoxicity of the CTAB surfactant, and high concentrations needed for conductivity. Using the most popular seed-mediated synthesis of GNRs, others have produced low aspect ratio GNRs (3–4) with low yields (~15% of Au<sup>3+</sup> ions were reduced to Au in nanorods) and often significant contamination of spherical or other shapes of particles.<sup>25,26</sup> Use of a bisurfactant growth solution enabled higher aspect ratio GNRs to be formed; however, the yields were still low.<sup>25</sup> We employed a robust and repeatable GNR synthesis by Vigderman and Zubarev<sup>17</sup> that used hydroquinone instead of the typically used ascorbic acid. Compared to the conventional ascorbic acid synthesis, the hydroquinone synthesis required more time (12 h vs. 3 h) but had higher yields (~80% in the current study, vs. the ~15% from the conventional ascorbic acid synthesis), higher aspect ratios (7 to 8 in the current study vs. 3 to 4 from the conventional ascorbic acid synthesis), and minimal contamination of other shapes (e.g., spheres, dog-bone shapes). While one study synthesized a gold nanowire hydrogel,<sup>27</sup> other gold nanorod hydrogels have utilized smaller aspect ratio CTAB-GNRs and similar, but slightly higher concentrations of the GNRs (e.g., 1.0 and 1.5 mg/ml<sup>11</sup> vs. our 0.6 and 0.8 mg/ml of GNRs). The high aspect ratio GNRs had not been combined with a biomaterial, therefore, we combined the high aspect ratio GNRs in a hydrogel to create a conductive hydrogel.

In the current study, the 0.6 and 0.8 mg/ml citrate-GNR concentrations were conductive (up to  $1.15 \times 10^{-5} \pm 0.19 \times 10^{-5}$  S/cm). Most GNR biomaterials, which have primarily been used in cardiac tissue engineering,<sup>11,12</sup> have been characterized by different methods (e.g., impedance) or not characterized at all. However, the conductivities of a few gold nanoparticle biomaterials have been measured ( $1 \times 10^{-4}$  to  $1.5 \times 10^{-1}$  S/cm<sup>28–30</sup>), and were higher than the GNR hydrogels developed in the current study. We speculate that the conductivity of the GNR hydrogels developed in the current study were lower because of the increased hydrogel swelling. Possibly, the postcrosslinking swelling may have caused the network of GNRs to expand and decrease GNR contact, and therefore decrease conductivity. Specifically, we speculate that the plateau of the conductivities at the higher 1.0 and 1.2 mg/ml concentrations may have been caused by inhibited crosslinking/increased swelling at higher GNR concentrations. The conductivity of the GNR hydrogels may be further improved in the future, such as through the addition of higher aspect ratio conductive components (e.g., gold nanowires), or other conductive components (e.g., graphene nanoribbons, poly[3,4-ethylenedioxythiophene] polystyrene sulfonate [PEDOT:PSS]).

While CTAB-GNRs have been used in hydrogels, to the best of our knowledge, nontoxic citrate-GNRs had not yet been combined with a hydrogel. Even with a robust, high-yield synthesis of high aspect ratio GNRs, one major limitation of GNRs in our studies was the cytotoxicity of the CTAB surfactant, which is required for shape

control and rod formation.<sup>13</sup> While Navaei et al.<sup>11</sup> found that CTAB-GNRs in methacrylated gelatin hydrogels were not cytotoxic for cardiomyocytes, our preliminary studies with PHA/PGel/CTAB-GNRs at various concentrations were highly cytotoxic within 1 day for seeded rNSCs (data not shown), presumably from the CTAB. Given the low efficacy of direct ligand exchange protocols for replacing CTAB on GNRs, an indirect ligand exchange protocol<sup>14</sup> was adapted by adjusting the silver to gold molar ratio and initial GNR concentration for successful exchange of CTAB for citrate. All of the PHA/PGel hydrogels with citrate-GNRs supported rNSC adhesion and viability, however, the rNSCs on the GNR hydrogels had lower DNA content than those on the PHA/PGel hydrogels. We speculate the lower DNA content was from partially inhibited adhesion of rNSCs to the GNR hydrogels. The rNSC spheroids on the bioprinted GNR hydrogels appeared to have a more spherical morphology than those on the PHA/PGel hydrogels, which were more spread on the hydrogels, specifically on the PGel patches. It is possible that the negatively charged citrate on the GNRs may repel the negatively charged cell membrane of rNSCs and partially inhibit adhesion to the hydrogel. Additionally, the rNSC spheroids on the bioprinted GNR hydrogels were comprised of mainly live cells and few dead cells, indicating that the lower DNA content on the GNR hydrogels were not from cytotoxicity. While rNSCs are known to lack CD44 and do not adhere to HA, the PHA in the hydrogel formulation is integral for extending the in vitro degradation time of the hydrogel, as PGel-only hydrogels completely degraded in <2 weeks in vitro with cells (data not shown) but PHA/PGel hydrogels maintained their integrity past 2 weeks in culture. Future study will include improving the adhesion of rNSCs to the GNR hydrogels, such as through the incorporation of fibronectin and/or laminin peptides (e.g., RGD, IKVAV, YIGSR) into the hydrogel.

There were several additional benefits of the citrate-GNRs relative to the CTAB-GNRs. First, given that citrate is known to be a better stabilizer than CTAB,<sup>31</sup> our results were consistent with others and there was less aggregation and an extended shelf-life of citrate-GNRs compared to CTAB-GNRs. Citrate-GNRs did not aggregate over time as quickly, compared to CTAB-GNRs that started partially aggregating within 1 to 2 days. Second, the enhanced stabilization and dispersion of citrate-GNRs enabled them to be sterile-filtered for in vitro studies, while retaining ~66% of the GNRs by mass. The CTAB-GNRs were not able to be sterile-filtered, even directly after synthesis, most likely from partial aggregation. Third, the better dispersion of citrate-GNRs enabled easier blending with the PHA/PGel precursor compared to the CTAB-GNRs. Mehtala et al.<sup>31</sup> similarly found that CTAB-GNRs were destabilized and resulted in partial aggregation after excess CTAB was removed. They successfully used a different indirect method using polystyrenesulfonate (PSS) to exchange the CTAB for citrate. In general, the focus of citrate-GNRs has been on the exchange of CTAB for citrate to enable further functionalization<sup>31</sup> or future use in biomedical applications,<sup>14</sup> not on sterilization methods, fabrication of conductive composites, or applications to bioprinting.

Finally, the GNR hydrogels had a paste-like rheology, which enhanced the surgical translation and bioprintability. Other reported

gold nanoparticle hydrogels have been developed and shown to be injectable, but the viscosity was not characterized.<sup>29,32,33</sup> The GNR precursor developed in the current study had a shear thinning viscosity profile, which enabled it to be injected through a nozzle for both bioprinting and easier surgical placement. Furthermore, the GNR precursor had a good storage modulus recovery (i.e.,  $\geq 80\%$ ) and an improved yield stress compared to the PHA/PGel, which led to higher shape fidelity of the bioprinted construct and may additionally improve retainment of the material after surgical injection into an SCI. One study bioprinted GelMA-GNRs in alginate hydrogels, but the bioprinting required the co-extrusion of the bioink with calcium chloride to form stable bioprinted struts.<sup>12</sup> Another study leveraged GNPs to slowly crosslink thiolated HA, thiolated gelatin, and PEG-diacrylate.<sup>34</sup> While the slow crosslinking (i.e.,  $> 24$  h) was suitable for bioprinting, it may not be suitable for surgical translation. Compared to previously bioprinted GNR or GNP hydrogels, the GNR hydrogel precursor developed in the current study was able to be bioprinted into stable struts without any support solutions and have controlled photo-crosslinking in 4 min, which enhanced bioprinting.

Additionally, the paste-like rheology of the GNR precursor enhanced surgical placement. The feasibility of delivering the GNR hydrogel and safety for the duration of a 2-month pilot study in rats was demonstrated, where rats received a T8 lateral hemi-section (see Figures S1–S3). The paste-like materials (i.e., PHA/PGel/GNR, PHA/PGel, PHA) were easier to use and were better retained in the injury during crosslinking compared to the liquid precursor of PGel. The GNR hydrogels were feasible to implant, and did not have toxic side effects on vital organs over 8 weeks (see Figure S3). While these initial studies ensured that the GNR hydrogels were nontoxic and verified that the GNR hydrogels had surgical clinical potential, future studies will be vital to compare the clinical potential in terms of neural regeneration and functional recovery, and specifically with and without ES.

In addition to the precursor characterization, the mechanical performance and swelling properties of the crosslinked hydrogels implanted into a SCI were important to characterize because swelling may result in increased intraspinal pressures, which in turn may result in negative clinical outcomes.<sup>35</sup> The GNR hydrogels had increased swelling and absorption of water, and we speculate the cause was limited crosslinking from the high GNR concentrations. Despite the higher aspect ratio GNRs, the GNR concentrations are high enough to limit crosslinking because of the dark color/opacity of the hydrogels and/or less available crosslinker. Thiols bond to gold quickly and with high affinity, which may have trapped some of the dithiol crosslinker and partially inhibited crosslinking of the PHA or PGel polymers. No visible aggregates were seen in the precursor, but GNR hydrogels had increased swelling and absorption, which was consistent with a less crosslinked network. Lower compressive elastic moduli typically accompany softer hydrogels; however, the GNR hydrogels did not have significantly different compressive moduli from the PHA/PGel hydrogels. Gold nanoparticles have been used in tissue engineering to generate hydrogels with improved stiffness,<sup>36</sup> therefore, we speculated that the GNRs may have increased the moduli of PHA/PGel, but

the inhibited crosslinking may have diminished or counterbalanced that effect. In the future, hydrogel crosslinking may be improved and swelling reduced by increasing the PHA functionalization, increasing the concentration of the DTT crosslinker, use of different nontoxic crosslinkers (e.g., peptide crosslinkers), or alternative crosslinking chemistries (e.g., methacrylate chemistry).

The rNSCs on the bioprinted GNR hydrogels had similar staining intensity and distribution for neural stem cells and neurons compared to the PHA/PGel, indicating that the GNR hydrogel by itself may not be promoting early neural differentiation. While rNSCs may be beginning to differentiate by day 7, we did not anticipate that GNR hydrogels by themselves would promote differentiation without ES, which highlights the importance of future studies of GNR hydrogels combined with ES. We hypothesize that the conductive hydrogel combined with ES will be necessary to drive neural differentiation. Given that HA hydrogels are insulators, few studies have applied electrical stimulation with HA hydrogels (e.g., cartilage repair,<sup>37</sup> peripheral nerve repair<sup>38</sup>), but the conductivity of the GNR hydrogel developed in the current study provided the conductivity that will enable it to be a platform to deliver ES directly to encapsulated cells in the future. These future studies will have the opportunity to explore parameters such as current intensity, frequency, and duration, and to investigate whether the GNR hydrogel will promote neural differentiation and/or neurite growth. Additional *in vivo* studies will then be warranted to investigate whether the GNR hydrogel, with and without ES, will promote axon regeneration and neural plasticity. Overall, conductive bioinks such as the GNR hydrogel developed in the current study are translational platforms that may synergistically link regenerative medicine and rehabilitation approaches for developing regenerative rehabilitation treatments for SCI.

## 5 | CONCLUSIONS

The goals of the study were accomplished with the development of a GNR hydrogel that was electrically conductive, nontoxic, and had an injectable, paste-like precursor that was bioprintable and enabled enhanced surgical placement for SCI. Two established protocols for a robust synthesis for high aspect ratio GNRs and an indirect ligand exchange were combined to produce nontoxic, high aspect ratio citrate-GNRs that overcome several of the challenges associated with GNRs and may enable widespread use of GNRs in other biomedical applications. No previous studies have applied a GNR-based conductive hydrogel for SCI, but the developed injectable and conductive GNR hydrogel provides a key translational platform that may be refined to promote *in vivo* neural regeneration and eventually used to synergistically combine regenerative medicine approaches and rehabilitation approaches (e.g., ES) to maximize functional recovery after SCI.

## ACKNOWLEDGMENTS

This study was supported by the University of Oklahoma (OU) Stephenson Graduate Fellowship (Emi A. Kiyotake); and the



National Science Foundation (NSF) Major Research Instrumentation (MRI) Program (Award #1828234) for the ICP-MS. We thank Dr. Yingtao Liu and Blake Herren for the conductivity testing protocol development and use of the Instron, the OU NMR Facility for the NMR, the OU Samuel Roberts Noble Microscopy Laboratory and Drs. Preston Larson and Tingting Gu for assistance with the TEM and confocal microscopy, respectively. We acknowledge Stephenson Cancer Center at the University of Oklahoma Health Sciences Center, Oklahoma City, OK and an Institutional Development Award (IDeA) from the National Institute of General Medical Sciences of the National Institutes of Health under grant number P20 GM103639 for the use of Histology and Immunohistochemistry Core, which provided histology and IHC services. We thank Larson Sewell for building the open field. We thank Boushra Ajeeb, M.S., for help with the gold nanorod synthesis and the members of the Translational Regenerative Medicine Lab for their support.

### CONFLICT OF INTEREST

The authors declare no conflict of interest.

### DATA AVAILABILITY STATEMENT

The data that support the findings of this study are available from the corresponding author upon reasonable request.

### ORCID

Emi A. Kiyotake  <https://orcid.org/0000-0002-6864-3753>

Emily E. Thomas  <https://orcid.org/0000-0003-4712-111X>

### REFERENCES

- National Spinal Cord Injury Statistical Center. *Facts and figures at a glance*. Birmingham, AL: University of Alabama at Birmingham; 2020:2020.
- Kiyotake EA, Martin MD, Detamore MS. Regenerative rehabilitation with conductive biomaterials for spinal cord injury. *Acta Biomater*. 2020. <https://doi.org/10.1016/j.actbio.2020.12.021>.
- Willett NJ, Boninger ML, Miller LJ, et al. Taking the next steps in regenerative rehabilitation: establishment of a new interdisciplinary field. *Arch Phys Med Rehabil*. 2020;101(5):917-923.
- Lin J, Anopas D, Milbreta U, et al. Regenerative rehabilitation: exploring the synergistic effects of rehabilitation and implantation of a bio-functional scaffold in enhancing nerve regeneration. *Biomater Sci*. 2019;7(12):5150-5160.
- Yarrow JF, Kok HJ, Phillips EG, et al. Locomotor training with adjuvant testosterone preserves cancellous bone and promotes muscle plasticity in male rats after severe spinal cord injury. *J Neurosci Res*. 2020;98(5):843-868.
- Palza H, Zapata PA, Angulo-Pineda C. Electroactive smart polymers for biomedical applications. *Materials (Basel)*. 2019;12(2):277.
- Ghasemi-Mobarakeh L, Prabhakaran MP, Morshed M, et al. Application of conductive polymers, scaffolds and electrical stimulation for nerve tissue engineering. *J Tissue Eng Regen Med*. 2011;5(4):e17-e35.
- Zhu R, Sun Z, Li C, Ramakrishna S, Chiu K, He L. Electrical stimulation affects neural stem cell fate and function in vitro. *Exp Neurol*. 2019; 319:112963.
- Navaei A, Moore N, Sullivan RT, Truong D, Migrino RQ, Nikkhah M. Electrically conductive hydrogel-based micro-topographies for the development of organized cardiac tissues. *RSC Adv*. 2017;7(6):3302-3312.
- Navaei A, Rahmani Eliato K, Ros R, Migrino RQ, Willis BC, Nikkhah M. The influence of electrically conductive and non-conductive nanocomposite scaffolds on the maturation and excitability of engineered cardiac tissues. *Biomater Sci*. 2019;7(2):585-595.
- Navaei A, Saini H, Christenson W, Sullivan RT, Ros R, Nikkhah M. Gold nanorod-incorporated gelatin-based conductive hydrogels for engineering cardiac tissue constructs. *Acta Biomater*. 2016;41: 133-146.
- Zhu K, Shin SR, van Kempen T, et al. Gold nanocomposite bioink for printing 3D cardiac constructs. *Adv Funct Mater*. 2017;27(12): 1605352.
- Zhang Y, Newton B, Lewis E, et al. Cytotoxicity of organic surface coating agents used for nanoparticles synthesis and stability. *Toxicol In Vitro*. 2015;29(4):762-768.
- Zhou S, Huo D, Goines S, et al. Enabling complete ligand exchange on the surface of gold nanocrystals through the deposition and then etching of silver. *J Am Chem Soc*. 2018;140(38):11898-11901.
- Townsend JM, Beck EC, Gehrke SH, Berkland CJ, Detamore MS. Flow behavior prior to crosslinking: the need for precursor rheology for placement of hydrogels in medical applications and for 3D bioprinting. *Prog Polym Sci*. 2019;91:126-140.
- Kiyotake EA, Douglas AW, Thomas EE, Nimmo SL, Detamore MS. Development and quantitative characterization of the precursor rheology of hyaluronic acid hydrogels for bioprinting. *Acta Biomater*. 2019;95:176-187.
- Vigderman L, Zubarev ER. High-yield synthesis of gold nanorods with longitudinal SPR peak greater than 1200 nm using hydroquinone as a reducing agent. *Chem Mater*. 2013;25(8):1450-1457.
- Donahue ND, Francek ER, Kiyotake E, et al. Assessing nanoparticle colloidal stability with single-particle inductively coupled plasma mass spectrometry (SP-ICP-MS). *Anal Bioanal Chem*. 2020;412(22):5205-5216.
- Lee JC, Donahue ND, Mao AS, et al. Exploring Maleimide-based nanoparticle surface engineering to control cellular interactions. *ACS Appl Nano Mater*. 2020;3(3):2421-2429.
- Herren BCharara MSaha MCAItan MC, Liu Y. Rapid microwave polymerization of porous Nanocomposites with Piezoresistive sensing function. *Nanomaterials (Basel)*. 2020;10(2):233.
- Townsend JM, Sali G, Homburg HB, et al. Thiolated bone and tendon tissue particles covalently bound in hydrogels for in vivo calvarial bone regeneration. *Acta Biomater*. 2020;104:66-75.
- Therriault D, White SR, Lewis JA. Rheological behavior of fugitive organic inks for direct-write assembly. *Appl Rheol*. 2007;17(1): 10112-1-10112-8.
- Ribeiro A, Blokzijl MM, Levato R, et al. Assessing bioink shape fidelity to aid material development in 3D bioprinting. *Biofabrication*. 2017; 10(1):014102.
- Beck EC, Barragan M, Tadros MH, Gehrke SH, Detamore MS. Approaching the compressive modulus of articular cartilage with a decellularized cartilage-based hydrogel. *Acta Biomater*. 2016;38:94-105.
- Nikoobakht B, El-Sayed MA. Preparation and growth mechanism of gold Nanorods (NRs) using seed-mediated growth method. *Chem Mater*. 2003;15(10):1957-1962.
- Orendorff CJ, Murphy CJ. Quantitation of metal content in the silver-assisted growth of gold nanorods. *J Phys Chem B*. 2006;110(9):3990-3994.
- Dvir T, Timko BP, Brigham MD, et al. Nanowired three-dimensional cardiac patches. *Nat Nanotechnol*. 2011;6(11):720-725.
- Baei P, Jalili-Firoozinehad S, Rajabi-Zeleti S, Tafazzoli-Shadpour M, Baharvand H, Aghdami N. Electrically conductive gold nanoparticle-chitosan thermosensitive hydrogels for cardiac tissue engineering. *Korean J Couns Psychother*. 2016;63:131-141.
- Pourjavadi A, Doroudian M, Ahadpour A, Azari S. Injectable chitosan/kappa-carrageenan hydrogel designed with au nanoparticles: a

- conductive scaffold for tissue engineering demands. *Int J Biol Macromol*. 2019;126:310-317.
30. You JO, Rafat M, Ye GJ, Auguste DT. Nanoengineering the heart: conductive scaffolds enhance connexin 43 expression. *Nano Lett*. 2011;11(9):3643-3648.
31. Mehtala JG, Zemlyanov DY, Max JP, Kadasala N, Zhao S, Wei A. Citrate-stabilized gold Nanorods. *Langmuir*. 2014;30(46):13727-13730.
32. Zhang Y, Fan W, Wang K, Wei H, Zhang R, Wu Y. Novel preparation of Au nanoparticles loaded Laponite nanoparticles/ECM injectable hydrogel on cardiac differentiation of resident cardiac stem cells to cardiomyocytes. *J Photochem Photobiol B*. 2019;192:49-54.
33. Nezhad-Mokhtari P, Akrami-Hasan-Kohal M, Ghorbani M. An injectable chitosan-based hydrogel scaffold containing gold nanoparticles for tissue engineering applications. *Int J Biol Macromol*. 2020;154:198-205.
34. Skardal A, Zhang J, McCoard L, Oottamasathien S, Prestwich GD. Dynamically crosslinked gold nanoparticle - hyaluronan hydrogels. *Adv Mater*. 2010;22(42):4736-4740.
35. Khaing ZZ, Ehsanipour A, Hofstetter CP, Seidlits SK. Injectable hydrogels for spinal cord repair: a focus on swelling and Intraspinal pressure. *Cells Tissues Organs*. 2016;202(1-2):67-84.
36. Yadid M, Feiner R, Dvir T. Gold nanoparticle-integrated scaffolds for tissue engineering and regenerative medicine. *Nano Lett*. 2019;19(4):2198-2206.
37. Vaca-Gonzalez JJ, Clara-Trujillo S, Guillot-Ferriols M, et al. Effect of electrical stimulation on chondrogenic differentiation of mesenchymal stem cells cultured in hyaluronic acid: gelatin injectable hydrogels. *Bioelectrochemistry*. 2020;134:107536.
38. Ramos CM, Barges MJM, Roca FG, et al. Electrical stimulation increases schwann cells proliferation inside hyaluronic acid conduits. 2018;2018(10-13):1-2.

#### SUPPORTING INFORMATION

Additional supporting information may be found online in the Supporting Information section at the end of this article.

**How to cite this article:** Kiyotake, E. A., Thomas, E. E., Homburg, H. B., Milton, C. K., Smitherman, A. D., Donahue, N. D., Fung, K.-M., Wilhelm, S., Martin, M. D., & Detamore, M. S. (2022). Conductive and injectable hyaluronic acid/gelatin/gold nanorod hydrogels for enhanced surgical translation and bioprinting. *Journal of Biomedical Materials Research Part A*, 110(2), 365-382. <https://doi.org/10.1002/jbm.a.37294>